AFRL-RV-PS-
TR-2018-0141

FULL WAVEFORM MODELING OF HIGH FREQUENCY REGIONAL PHASES FOR OPTIMIZATION OF REGIONAL MONITORING

Vernon F. Cormier
Christopher Sanborn

University of Connecticut
Department of Physics
2152 Hillside Road
Storrs, CT 06269-3046

16 July 2018

Final Report

AIR FORCE RESEARCH LABORATORY
Space Vehicles Directorate
3550 Aberdeen Ave SE
AIR FORCE MATERIEL COMMAND
KIRTLAND AIR FORCE BASE, NM 87117-5776

DTIC COPY

NOTICE AND SIGNATURE PAGE

AFRL-RV-PS-TR-2018-0141 HAS BEEN REVIEWED AND IS APPROVED FOR PUBLICATION IN ACCORDANCE WITH ASSIGNED DISTRIBUTION STATEMENT.

//SIGNED//	//SIGNED//
Dr. Frederick Schult	Dr. Thomas R. Caudill, Chief
Program Manager/AFRL/RVBYE	AFRL Geospace Technologies Division

REPORT DOCUMENTATION PAGE

Form Approved
OMB No. 0704-0188

1. REPORT DATE *(DD-MM-YYYY)*	**2. REPORT TYPE**	**3. DATES COVERED** *(From - To)*
16-07-2018	Final Report	25 Jun 2015 – 30 June 2018

4. TITLE AND SUBTITLE
Full Waveform Modeling of High Frequency Regional Phases for Optimization of Regional Monitoring

5a. CONTRACT NUMBER
FA9453-15-C-0069

5b. GRANT NUMBER

5c. PROGRAM ELEMENT NUMBER
62601F

6. AUTHOR(S)
Vernon F. Cormier and Christopher Sanborn

5d. PROJECT NUMBER
1010

5e. TASK NUMBER
PPM00019929

5f. WORK UNIT NUMBER
EF127553

7. PERFORMING ORGANIZATION NAME(S) AND ADDRESS(ES)
University of Connecticut
Department of Physics
2152 Hillside Road
Storrs, CT 06269-3046

8. PERFORMING ORGANIZATION REPORT NUMBER

9. SPONSORING / MONITORING AGENCY NAME(S) AND ADDRESS(ES)
Air Force Research Laboratory
Space Vehicles Directorate
3550 Aberdeen Avenue SE
Kirtland AFB, NM 87117-5776

10. SPONSOR/MONITOR'S ACRONYM(S)
AFRL/RVBYE

11. SPONSOR/MONITOR'S REPORT NUMBER(S)
AFRL-RV-PS-TR-2018-0141

12. DISTRIBUTION / AVAILABILITY STATEMENT

Approved for public release; distribution is unlimited. (AFMC-2019-0096 dtd 11 Feb 2019)

13. SUPPLEMENTARY NOTES

14. ABSTRACT

Radiative transport modeling combines the effects of both large-scale and small-scale structure on the envelopes of high frequency regional seismograms. We describe a computer code that propagates packets of seismic body wave energy along ray paths through large-scale deterministic 3-D structure, and small scale heterogeneities. These techniques are applied to earthquakes and explosions recorded in the Lop Nor, China region to model observed narrow band passed seismic codas in the 1 to 4 Hz band. To investigate the effects of laterally varying Earth structure on the efficiency of propagation of Lg and Pg, we apply radiative transport to model regional coda envelopes to predict the effects on waveforms of paths crossing regions of crustal thinning (pull-apart basins and ocean/continent transitions) and thickening (collisional mountain belts). Using envelopes of regional high frequency seismograms synthesized by radiative transport algorithm, we investigate tradeoffs in model parameters describing a von Kármán heterogeneity spectrum and intrinsic attenuation of the crust.

15. SUBJECT TERMS

radiative transport, seismic scattering, seismic coda, Lg blockage

16. SECURITY CLASSIFICATION OF:			**17. LIMITATION OF ABSTRACT**	**18. NUMBER OF PAGES**	**19a. NAME OF RESPONSIBLE PERSON**
a. REPORT	**b. ABSTRACT**	**c. THIS PAGE**			Dr. Frederick Schult
Unclassified	Unclassified	Unclassified	Unlimited	70	**19b. TELEPHONE NUMBER** *(include area code)*

This page is intentionally left blank.

Table of Contents

List of Figures

List of Tables

1. SUMMARY

Radiative transport modeling can combine the effects of both large-scale (deterministic) and small-scale (statistical) structure on the coda envelopes of high frequency regional seismograms. We describe a computer code that propagates packets of seismic body wave energy along ray paths through large-scale deterministic 3-D structure, including the effects of velocity gradients, intrinsic attenuation, source radiation pattern, and multiple scattering by layer boundaries and small scale heterogeneities specified by a heterogeneity spectrum. The spatial distribution of these energy packets can be displayed as time snapshots to aid in the understanding of regional phase propagation or displayed as a coda envelope by summing at receiver bins. These techniques are applied to earthquakes and explosions recorded in the Lop Nor, China region to model observed narrow band passed seismic codas in the 1 to 4 Hz band. We predict that source discriminants in this region based on P/Lg amplitude ratios will best separate earthquake and explosion populations at frequencies 2 Hz and higher.

To investigate the effects of laterally varying Earth structure on the efficiency of propagation of Lg and Pg, we apply radiative transport to model regional coda envelopes. Seismograms of explosion and earthquake sources are synthesized in canonical models to predict effects on waveforms of paths crossing regions of crustal thinning (pull-apart basins and ocean/continent transitions) and thickening (collisional mountain belts), For paths crossing crustal thinning regions, Lg is amplified at receivers within the thinned region but strongly disrupted and attenuated at receivers beyond the thinned region. For paths crossing regions of crustal thickening, Lg amplitude is attenuated at receivers within the thickened region, but experiences little or no reduction in amplitude at receivers beyond the thickened region. The length of the Lg propagation within a thickened region and the complexity of over- and under-thrust crustal layers, can produce localized zones of Lg amplification or attenuation. Regions of intense scattering within laterally homogeneous models of the crust increase Lg attenuation but do not disrupt its coda shape.

Using envelopes of regional high frequency seismograms synthesized by radiative transport algorithm, we investigate tradeoffs in model parameters describing a von Kármán heterogeneity spectrum and intrinsic attenuation of the crust. Simulations of waveform envelopes and examination of probability density functions that control scattering directions, mean free paths, and polarizations confirm that the velocity fluctuation parameter ε and the corner parameter a" of the von Kármán spectrum trades-off such that the product $\varepsilon^2 a$ is constant when the wavenumber k and scale length a" are on the order of $ka = 1$. Radiative transport methods of efficiently simulating waveform envelopes for large domains of heterogeneity and intrinsic attenuation make possible routine application of multiple-time-lapse window analysis (MLTWA) to separate intrinsic attenuation and scattering attenuation. The combination of parameters describing the heterogeneity spectrum and intrinsic attenuation can be minimized by seeking the frequency band in which seismic albedo is maximum, and fitting observations of waveform envelopes in a series of narrow pass bands in frequency.

2. INTRODUCTION

Radiative transport modeling combines the effects of both large-scale and small-scale structure on the envelopes of high frequency regional seismograms. We describe a computer code that propagates packets of seismic body wave energy along ray paths through large-scale deterministic 3-D structure, and small scale heterogeneities. These techniques are applied to earthquakes and explosions recorded in the Lop Nor, China region to model observed narrow band passed seismic codas in the 1 to 4 Hz band.

To investigate the effects of laterally varying Earth structure on the efficiency of propagation of Lg and Pg, we apply radiative transport to model regional coda envelopes to predict the effects on waveforms of paths crossing regions of crustal thinning (pull-apart basins and ocean/continent transitions) and thickening (collisional mountain belts).

Using envelopes of regional high frequency seismograms synthesized by radiative transport algorithm, we investigate tradeoffs in model parameters describing a von Kármán heterogeneity spectrum and intrinsic attenuation of the crust.

3. METHODS, ASSUMPTIONS, AND PROCEDURES

The term *coda* for the envelope of complex arrivals following direct P and S waves at local and regional distances originated with work by (Aki, 1969) who recognized their origin to be due to multiple scattering by small-scale (relative to wavelength) heterogeneities in the crust and lithosphere (Aki and Chouet, 1975). The radiative transport algorithm models these coda envelopes by simulating the diffusive transport of elastic energy through processes of multiple scattering in a medium having random fluctuations in elastic properties. Gusev and Abubakirov (1987) extended applications of radiative transport to elastic scattering using a Monte Carlo technique for tracking multiply scattered particles of elastic energy. Extensions to realistic Earth models followed in the work of Hoshiba (1997), who included particle interactions with layer boundaries, Yoshimoto (2000), who included effects of velocity gradients within layers, and Margerin et al. (2000), who elaborated treatment of S wave polarization. Hoshiba (1993) developed an analysis method (MLTW) now in common use for measuring the relative contributions of intrinsic versus scattering attenuation from the shape of seismic codas. Comprehensive reviews of seismic radiative transport modeling include the text by Sato et al. (2012) and an AGU monograph chapter by Margerin (2005). Przybilla et al. (2009) compared the method against finite-difference synthetics in 3-D, validating body wave coda predictions of the radiative transport method. Our implementation of the radiative transport algorithm in the code Radiative3D (Sanborn et al., 2017) largely follows that of Shearer and Earle (2008), who have applied it to teleseismic coda. Our code has been designed for observations of complete, 3-component, seismograms observed at regional distances. It allows for the input of moment tensor sources and complex, multi-layered, 3-D crust and upper mantle models with generalized spatial gradients in model cells.

3.1 Advantages of radiative transport

Radiative transport simulates the effects of small-scale structure without the need for model meshes that are dense enough to explicitly describe that structure. Instead, the model mesh describes only the large-scale, long-wavelength equivalent ($ka >> 1$) background medium, against which small-scale heterogeneities are assumed as a random perturbation field. Although rarely exploited, the large-scale background model may be fully 3-D. As long as the *scale* length of the reference medium is much larger than the wavelength, elastic wave propagation can be described by ray theory. The scale length is measured by maximum of the ratio of elastic velocity or density divided by its spatial gradient. Small-scale heterogeneities are described via a small number of statistical parameters. The effect of small-scale heterogeneities on propagation is handled by assuming they scatter an incident ray-theoretical field into different directions after traveling a mean free path. The radiation pattern of scattering is treated as a probability density from which a new propagation direction is selected. Both the scattering radiation patterns and mean free paths are functions of the heterogeneity spectrum.

3.2 Construction of models

Background large-scale models consist of first-order discontinuities with topography separating layers having 3-D variation of velocities and densities interpolated over a course grid, and a perturbed statistical component, specified by a heterogeneity spectrum parameterized by the power of velocity and density fluctuation and a small number of spectral shape parameters (Figure 1).

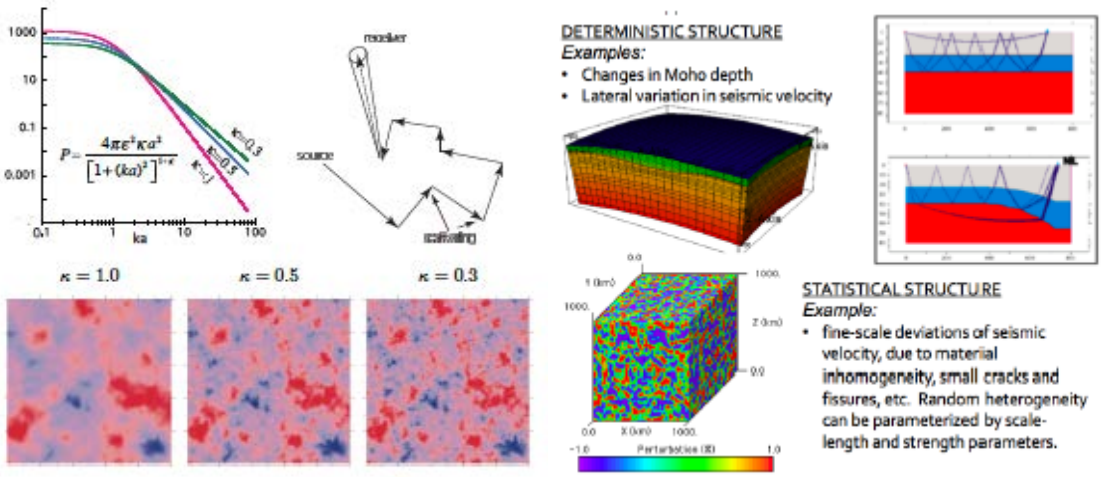

Figure 1. Model construction. *Top left: an example 2-D von Karman power spectrum of heterogeneity with variable k parameter that controls the decay of small-scale heterogeneity. Bottom left: medium realizations showing the effects of the k parameter. Right: 3-D examples of large-scale deterministic structure and small-scale statistical structure, including an example of the effect of crustal thickness variations on post-critical SmS rays that comprise the Lg wave trapped in the crustal waveguide.*

Significant advances have occurred in statistical characterization and understanding of such heterogeneity. Goff et al. (1994) described a procedure by which models having the spatial statistics of polycrystalline or multi-modal assemblages of rocks can be generated. Work beginning with Levander et al. (1994) and Pullammanappallil et al. (1997) makes it possible to formulate statistical models for common sedimentary and metamorphic formations. Model statistics can be modified as needed to reproduce the three-component behavior of the coda of regional seismic phases. Strong emphasis is placed on correctly characterizing the statistics of small-scale heterogeneities in the upper, highly heterogeneous, 10~km of the earth, which may correlate with the depth to a brittle to ductile transition in the crust (Rachman and Chung, 2016). Small-scale statistics affect the partitioning of P and S energy on the three-components of motion by the effects of scattering near the source and receiver. These small-scale statistics can strongly affect the performance of discriminants tuned to differences in sources occurring at the depths of contained nuclear tests.

Lateral variations in crustal thickness, basin depths, mountain roots, and lateral tectonic transitions also significantly affect the phases used for discrimination and detection. One example is the study by Pedersen et al. (1998), who explain anomalous Rayleigh to Love

mode conversion from Lop Nor explosions by changes in crustal thickness at the boundary of the Tarim Basin and Tian Shan mountain belt. Moho topography and basin thickness can also strongly affect the propagation of Lg (Cormier and Anderson, 2004). The scale of these types of lateral structural variations is often large enough to be resolvable by local and regional reflection and refraction experiments, gravity and magnetic data, regionalization by surficial geology, and global surface wave inversions. Hence, we refer to these types of structures as deterministic. The types of data used to infer deterministic structure are collected at widely different spatial scales, presenting a challenge to the parameterization of a three-dimensional model appropriate for a region surrounding a particular seismic station. The parameterization should be flexible enough to be specified at high-resolution where data is available and at lower resolution where it is not. Resolution should be high to describe features important to regional wave propagation, such as Moho and basin topography, but can be lower near interfaces having smaller velocity contrasts and lower with increasing depth in the mantle, where heterogeneity power decreases.

3.3 Software package

Our code Radiative3D is a tool for seismic radiative transport modeling with flexible Earth model and moment-tensor source input. The simulation engine includes deterministic ray tracing for longitudinal and shear propagation modes for generalized spatial gradients of elastic velocities in model cells, stochastic scattering controlled by heterogeneity parameters, reflection and transmission handling at sharp boundaries, and attenuation modeling from internal friction. Radiative3D produces output suitable for visualization with external tools. The output capabilities fall into two major categories: (1) event reporting, and (2) seismic energy binning. Event reporting means reporting the progress of individual phonons in a play-by-play manner. Examples of events in this context include: generation, scattering, crossing a model boundary, free-surface or discontinuity interface reflection and transmission, etc., or simply reporting the position of each phonon at regular time intervals. When these events are analyzed in post-processing, detailed pictures of energy propagation can be constructed. One of the first visualization tools developed was a GNU Octave script to produce videos illustrating P and S energy propagation in the Earth model (e.g., Figure 2). We have made Radiative3D available to the scientific community as a free and open-source software product (http://rainbow.phys.uconn.edu/geowiki/Radiative3D).

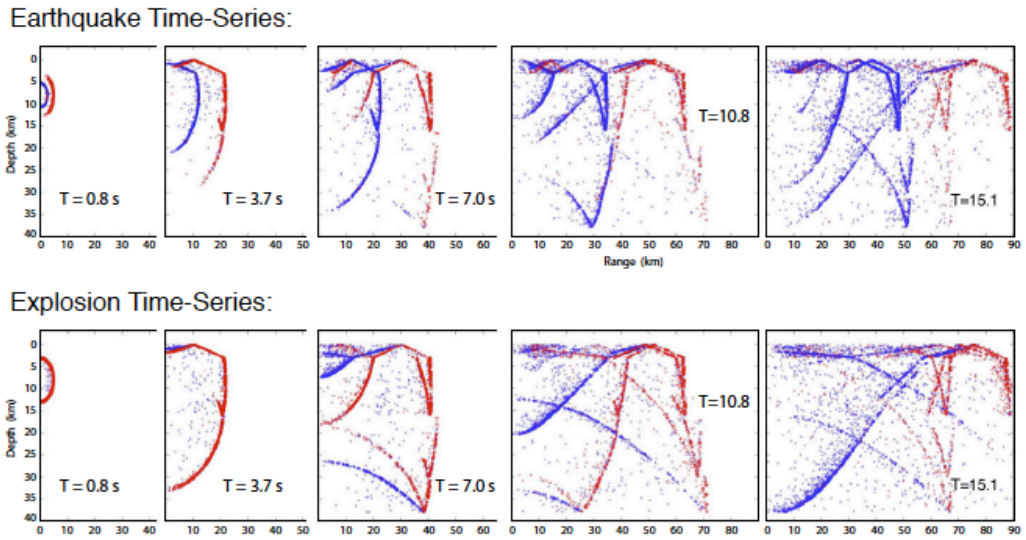

Figure 2. Wavefield snapshots. *Energy propagation visualized as a time series plot of phonon locations in a model cross section. Note the initial absence of the S wavefronts (blue) in the explosion time-series and its progressive development with time due to multiple scattering and interaction with the free surface.*

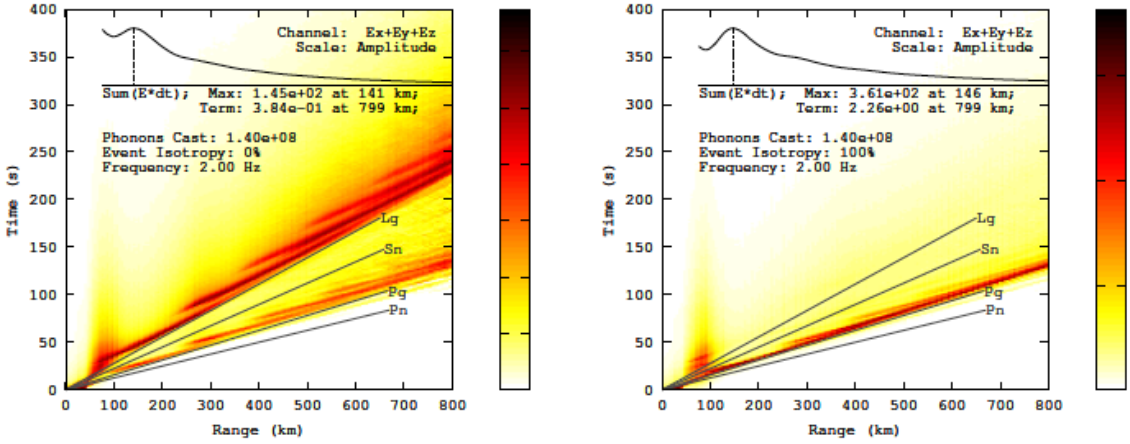

Figure 3. Travel time displays. *Travel time curves produced by Radiative3D for shallow focus earthquake (left) and explosion (right), Image density is proportional to the square root of energy flux arriving on all three axes, thus depicting an amplitude-like signal. A range-varying normalization curve is applied to the amplitudes so that the seismic phases remain distinct at all ranges. The normalization point is the mid-point between the average value and the peak value of the envelope at each distance range, and provides for good visual separation of phases. An overlay plot shows the time-integrated energy flux plotted on a square-root scale against range to show the overall amplitude decay with distance, omitting the very near range. Annotations identify the maximum of this integrated energy value and the value at the terminal range. Additionally, as with the envelope plots, the number of phonons cast, the frequency of the simulation, and isotropy of the event source are noted. Phase markers denoting the group velocities of the four regional phases are also shown for reference.*

Radiative3D allows for the placement of virtual seismometers along any surface designated as a collection surface. Whenever a phonon interacts with a collection surface within a specified gather radius of a seismometer, the energy of that phonon is recorded by the seismometer, decomposed into three Cartesian energy axes, and binned into time windows. At the end of simulation, these energy bins are output and can be interpreted as seismic energy traces, suitable for making envelope plots (see Example Application). Traces from multiple seismometers arranged in a linear array can be combined to make travel-time curves (e.g., Figure 3). Image density is proportional to the amplitude signal described above. A range-varying normalization curve is applied to the amplitudes so that the seismic phases remain distinct at all ranges. Thus, the image density is not proportional to absolute amplitude, but is relative to the normalization point. These plots allow the identification of seismic phases based on group velocity and time offset.

4. RESULTS AND DISCUSSION

4.1 Example Applications

4.1.1 Lop Nor

The Lop Nor, China region (Figure 4) is one of few regions in which nuclear tests and earthquake waveforms are well recorded at accessible global seismic stations and networks. More than half of the earthquakes in the Reviewed Event Bulletin (REB) of IMS occurred within 100~km of six Lop Nor test sites from 2000 through 2008 (Sykes and Nettles, 2009). LANL has also constructed maps of regional wave propagation efficiencies in this region (Phillips et al., 1999). Lop Nor is located near the southeastern side of the Tian Shan, a region of moderate earthquake activity and contemporary horizontal compressive stress in the earth's crust, which can be an important factor in inducing tectonic release from underground nuclear tests in this region.

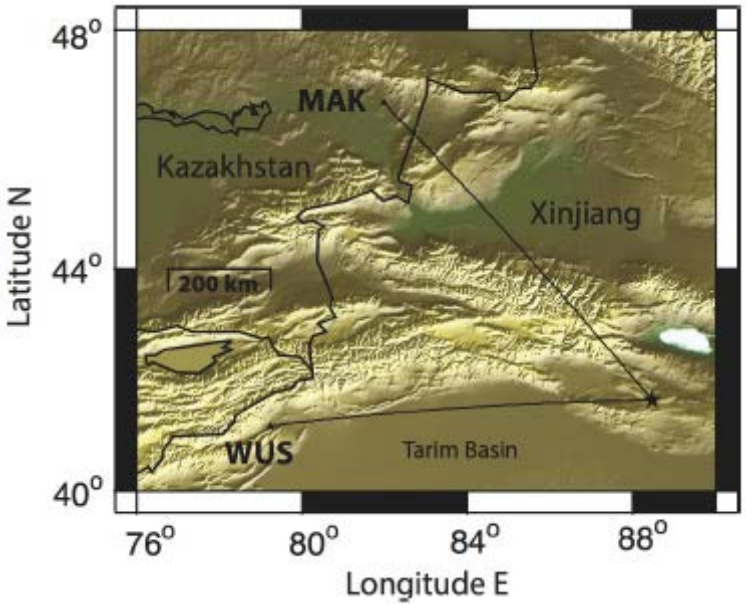

Figure 4. Lop Nor test site region. *Lop Nor test site and paths to regional seismic stations MAK and WUS on which we have concentrated modeling tests.*

The Chinese station WMQ (Urumqi) is about 250~km (2.15^{o}) from Lop Nor. Stations MAK and WUS are about 760~km (6.85^{o})from Lop Nor. For the earthquake and explosion data we use seismograms from events downloaded from IRIS-DMC.

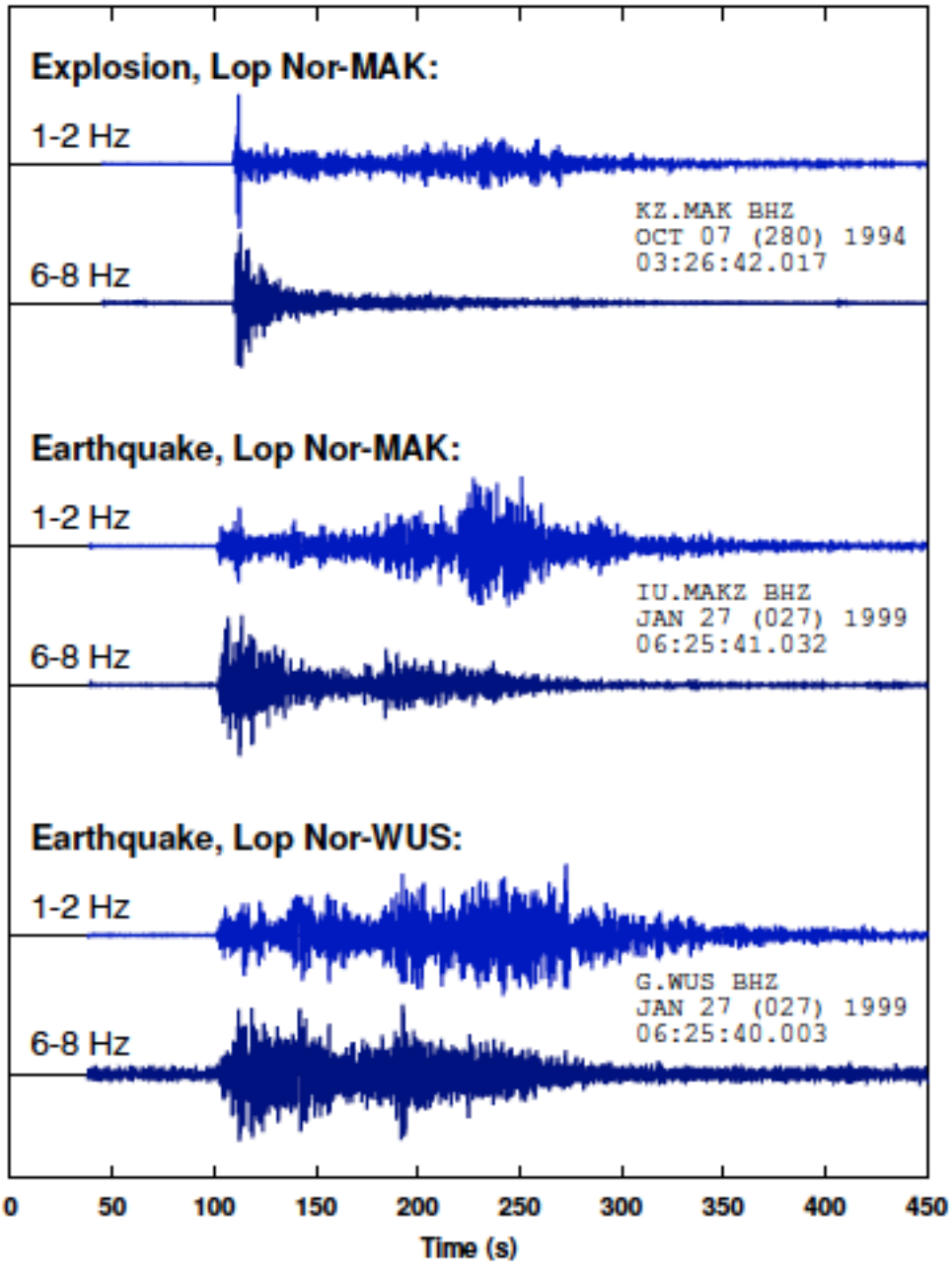

Figure 5. Waveforms recorded in the Lop Nor Region. *Vertical component band-passed data recorded at stations WUS and MAK in the Lop Nor region.*

The data in Figure 5 come from an explosion at the Lop Nor site as recorded at station MAK at great circle distance 6.85^{o} and an earthquake in the same area recorded at both

MAK and WUS. WUS is approximately at the same distance from Lop Nor as MAK but at a different azimuth. Data has been band passed between 1-2 Hz and between 6-8 Hz for each recording. Not only are there differences between the earthquake and explosion data at MAK, there are also differences between the earthquake traces at MAK and WUS in the time windows commonly used to measure Pn/Lg and Pg/Lg amplitude ratios.

4.1.2 Deterministic model

Using known elevations of Lop Nor and seismic stations MAK and WUS, along with Moho depths from the Cornell Moho model (atlas.geo.cornell.edu/geoid/imagegrid.html) and layer profiles from CRUST 2.0 (Laske et al., 2011) at those same locations, we located and oriented a set of five crust layers (sediments, upper, middle, and lower crust, and top layer of the mantle). Additionally, we defined an additional 16 mantle layers from AK-135-F (Kennett et al., 1995) and regionalized perturbations (Gudmundsson and Sambridge, 1998) to a depth of 859 km. These layers served as an initial deterministic background model (Figure 6) in which to run synthetics. Although our software is capable of simulating laterally-varying models that include velocity gradients defined on a tetrahedral mesh, we used only models consisting of layers of uniform background and statistical parameters in the present work. Gradient-like structures were approximated as a succession of layers varying in stair-step fashion. In models of this construction, phonon trajectories are straight lines, and scattering mean free paths are spatially stationary within individual layers. Reflection and refraction occur at interfaces between layers.

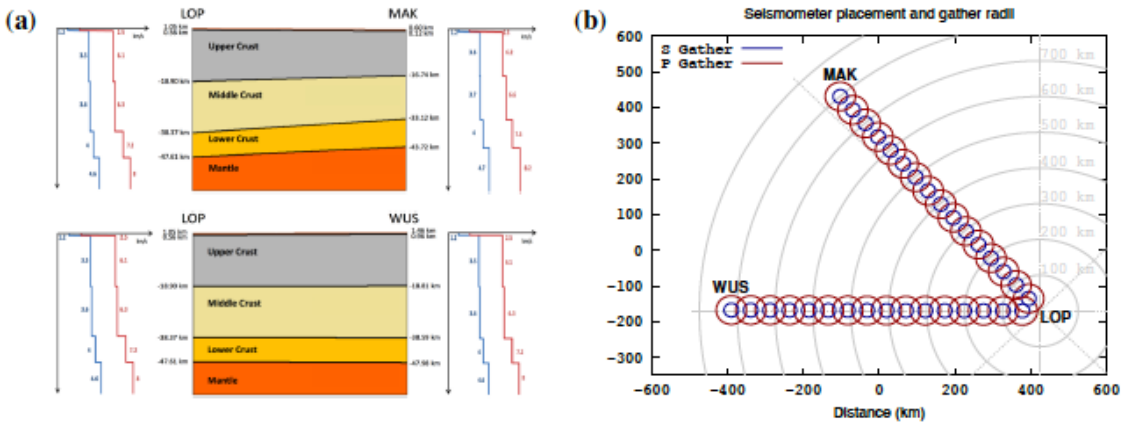

Figure 6. Lop Nor deterministic model and source/receiver configuration. *(a) Simplified Lop Nor Earth model composed of layers of uniform background velocity separated by planar tilted interfaces oriented to match depth profiles at Lop Nor, station MAK, and station WUS. A thin sediment layer (0.5~km) is included and sits on top of three crust layers extending to an average depth of 45 km, and 16 mantle layers down to a depth of 859 km. (b) Map view showing relative locations of Lop Nor, MAK, and WUS in model coordinates and two virtual seismometer arrays represented by gather-radius circles. Each array consists of 160 evenly spaced seismometers of which every tenth one is shown. Results presented here will focus on the LOP to MAK path.*

4.1.3 Statistical model

To determine our statistical model for the Lop Nor region, we first performed a series of experiments to examine the sensitivity of regional phases to the shape of the heterogeneity spectrum. These tests included tests to determine regional phase sensitivity to depth regions of the deterministic model as well as tradeoffs between parameters describing the heterogeneity spectrum and intrinsic attenuation (see Tradeoffs and Sensitivity). Spectral shape parameters were varied for a von Kármán spectrum. The advantage of this spectrum is that it can incorporate a more realistic medium behavior over a broad band of wavenumbers, reproducing a fractal-type behavior beyond a corner wavenumber (Margerin and Nolet, 2003). The parameters varied are: the fractional fluctuation ε of seismic wave velocities; a parameter ν controlling the density perturbation as a factor multiplying the P velocity fluctuation; a scale length *a* that controls the wave number corner; and a von Kármán Hurst order number κ that controls the slope of the power spectrum after its corner. Table 1 reports heterogeneity spectrum and attenuation parameters used for in our best fits to Lop Nor waveforms. The intrinsic Q_P for P waves is assumed to be 9/4 Q_S.

Table 1. Heterogeneity and attenuation parameters used in Lop Nor modeling.

	ν	ϵ	a	κ	Q_S
Sediments	0.8	0.01	0.25 km	0.2	50
Crust	0.8	0.04	0.2 km	0.3	2000
Transition	0.8	0.008	0.2 km	0.5	4000
Mantle	0.8	0.008	0.2 km	0.5	1200

4.1.4 Model features for Pn and Sn propagation

High frequency Pn and Sn are traditionally thought of as head waves traveling just beneath the Moho discontinuity. Early attempts to model high frequency Pn and Sn as classical head waves failed because the amplitude of a classical head wave decays with frequency 1/ω. These phases are now recognized as interference head waves (Cerveny and Ravindra, 1971). Interference head waves have a representation as series of body waves that are multiply reflected along the underside for either a Moho following Earth's curvature or for velocities that increase with depth beneath the Moho. Our initial experiments assumed a flat earth and homogeneous layers, separated by planar tilted interfaces. In these models energy does not return from the mantle except as scattered waves. With a series of stair-step discontinuities, we have simulated the effects of Earth curvature via an earth-flattening transformation and positive velocity gradients with decreasing radius (Figure 7). These modifications allow Pn and Sn to return to the surface after being multiply reflected by and scattered beneath the Moho. Additionally, intrinsic Q values were increased in the crust layer and below, as we found this improved match quality. Envelopes were synthesized for the 2003-03-13 southern Xinjiang earthquake (mb 4.8) recorded at MAK for this Moho model. Figure 8 shows envelope and travel

time results of this experiment with scattering from the reference statistical model turned on and off. New sharp arrivals preceding the Pg and Lg phases are visible in the envelope results. Inspection of the travel time curves confirms that these peaks have phase velocities consistent with Pn and Sn phases.

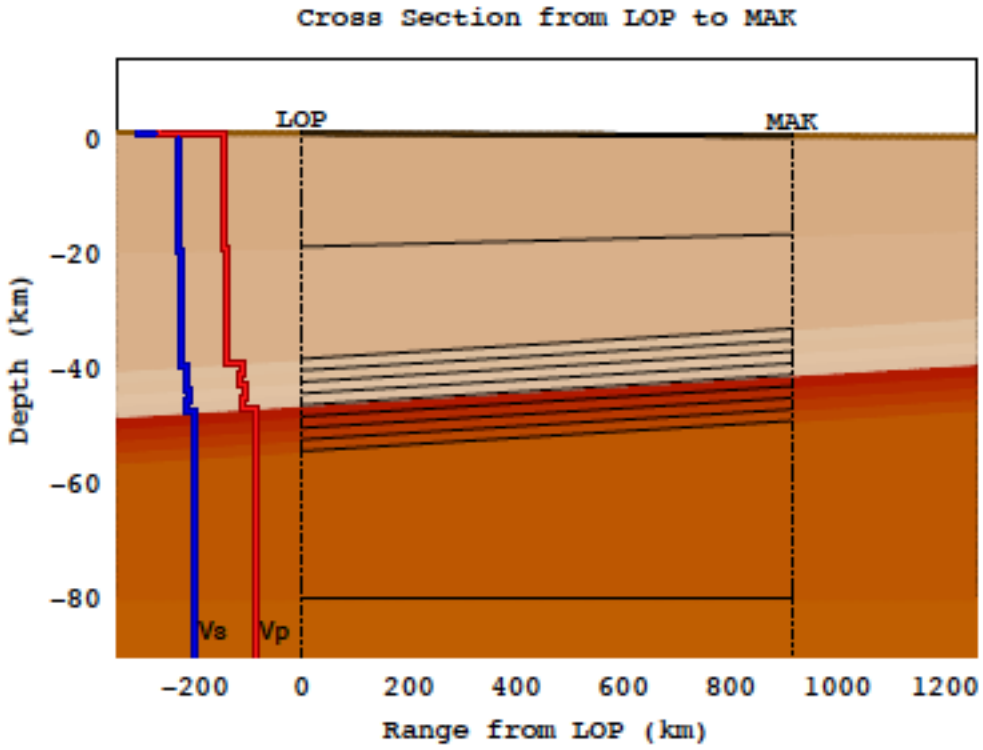

Figure 7. Model of Moho transition in Lop Nor region. *Earth model having a Moho transition region at the base of the crust and a very slight stair-step ramp at the top of the mantle for a path from a southern Xinjiang earthquake to station MAK. Depth dependences of P and S velocities are also shown. For simulations that included scattering, ε was 4% in the crust and 0.8% in the transition region and mantle. Simulations performed in this model had an earth-flattening transformation applied on input to the software to enhance effects of the stair-step gradients and mimic effects of Earth curvature. There is a thin (0.5 km) low velocity sedimentary layer at the top of the model.*

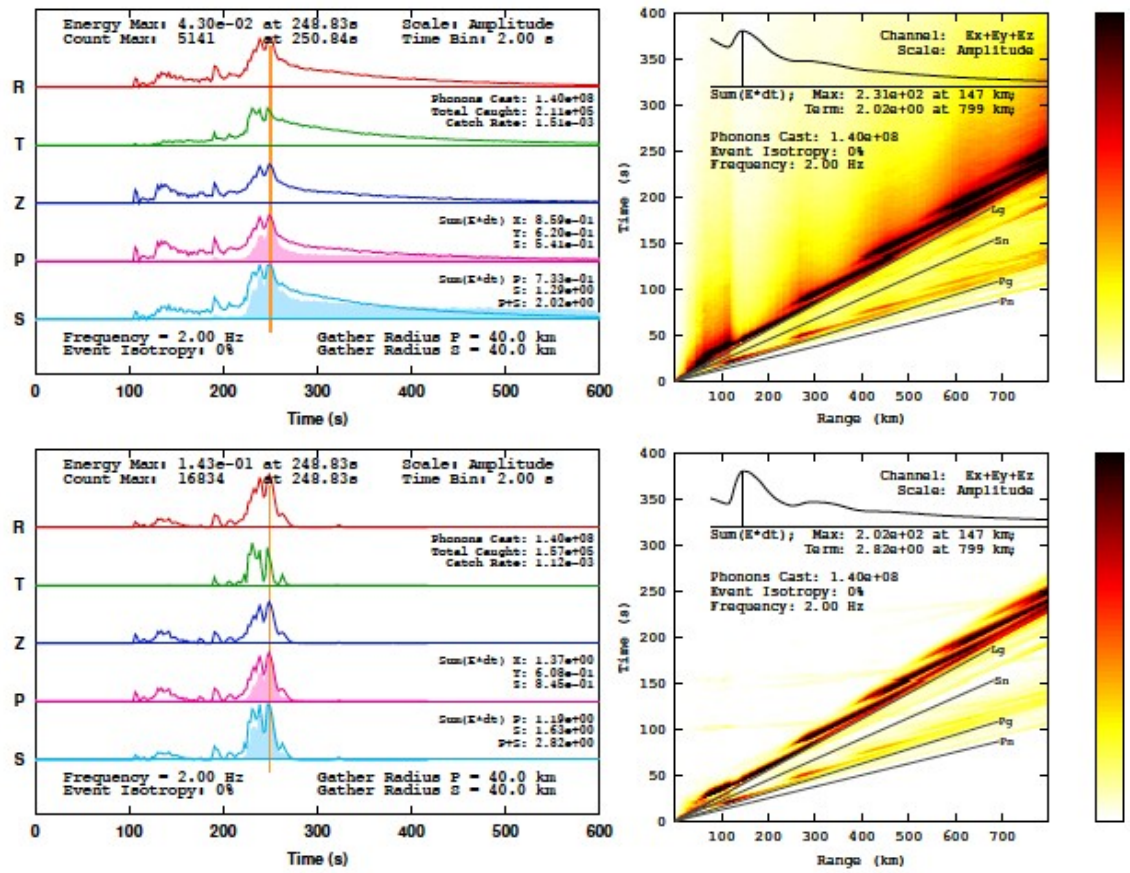

Figure 8. Synthetic envelopes and travel time curves for varying Moho structure. *Top: Synthetic envelopes for the Moho transition model (Figure 7) for the path to station MAK from a focal mechanism patterned after the 2003-03-13 southern Xinjiang earthquake (strike, dip, rake: 125°, 40°, 90° ; depth 6 km) with scattering predicted from the heterogeneity parameters in Table 1. Bottom: synthetic envelopes for the same path with scattering turned off.*

4.1.5 Observed and modeled earthquake

Figure 9 compares the synthetic z-component envelope that includes scattering against the recorded earthquake. The approximate arrivals of the four regional phases are marked. There is good agreement in arrival time and relative amplitude for the Pn and Lg phases. The Pg phase is overly sharp in the synthetic but more diffuse in the recording, although peak amplitudes are in good agreement. The Sn peak in the synthetic leads the corresponding peak in the recording by about 10~s and under-represents the relative amplitude by about 20%, but is otherwise in good agreement. Lastly, the rate of Lg coda decay is too gradual, indicating intrinsic Q values may be too high. We believe that better agreement may be achieved by tuning intrinsic Q values as well as extending the Moho transition region a bit further into the upper mantle, adding more layer divisions in that region so that the gradient-enhancing effect of the Earth-flattening transformation can more effectively enhance ray-turning potential, thereby increasing complexity in the Pn, Pg and Sn phases that sample or are affected by that region.

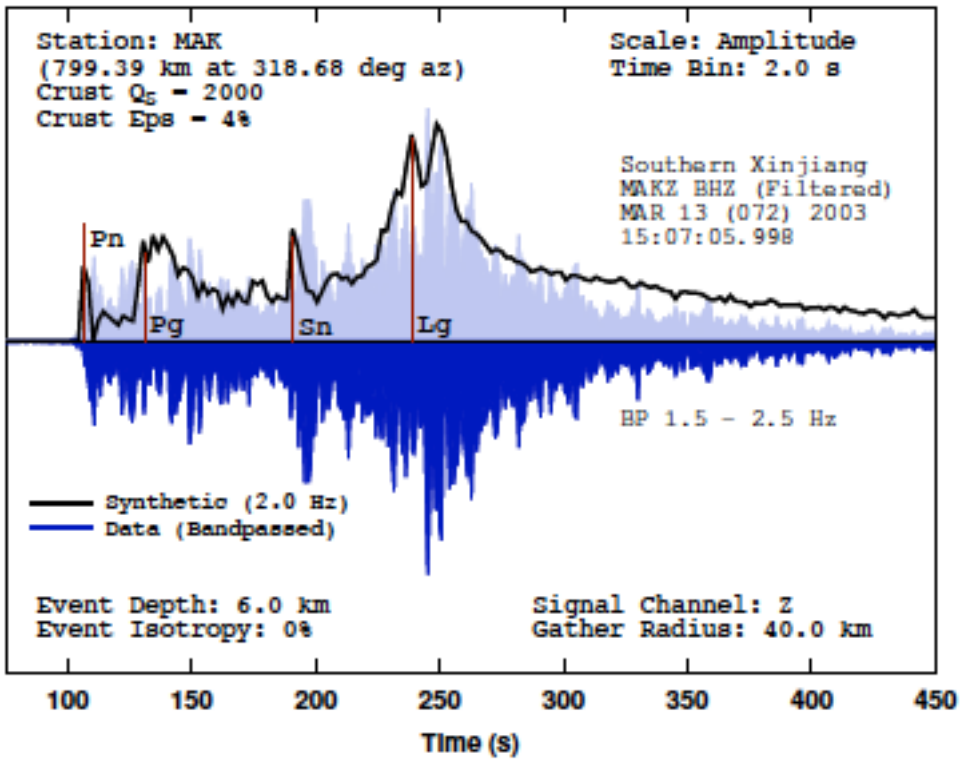

Figure 9. Synthetic and observed waveform envelope for Lop Nor earthquake. *Comparison of filtered recorded data with a 2.0 Hz synthetic coda envelope for a model having a Moho transition layer. Data is band passed from 1.5 to 2.5 Hz, enveloped, and mirrored across the x axis. The approximate arrivals of the regional phases are marked.*

4.1.6 Synthetics and data by frequency band

Radiative3D is run at a single frequency and can create simulated seismogram envelopes at any frequency. This allows analysts to interpret the structural or source origin of frequency-specific effects on narrow band passed seismic traces. Although the radiative transport algorithm assumes ray trajectories are independent of frequency, it incorporates the effects of scattering and intrinsic attenuation through functions that are frequency dependent. Additionally, source-spectral effects can be modeled by applying a weight function to single-frequency envelopes and combining these into a broad-band envelope after simulation.

There is now a substantial body of empirical evidence that regional P/S ratios provide poor discrimination below some frequency, typically about 2 to 3 Hz, and useful discrimination at higher frequencies, (Fisk, 2006). Hence, in Figure 10 we compare computed envelopes against narrow band passed data at 2, 3, and 4 Hz. The traces presented show a good general agreement between the synthetics and the data in: (1) the apportionment of energy between the Pg, Pn, Lg, and Sn windows, favoring Lg at 2.0 Hz but Pg and Pn at 4.0 Hz; and (2) the overall amplitude decay from the 2.0 Hz to 4.0 Hz bands. Although our modeled crustal shear Q value (2000) is higher than the coda Q values (731to 951) predicted by (Martynov, 1999) in this frequency band from

observations in the nearby Tian Shan region, we point out that our Q values are intrinsic Q values modeling thermal losses, and that the contribution from scattering will result in a lower effective Q value. In fact, we can estimate this effective Q value by assuming it is the inverse sum of intrinsic and scattering Q values, or

$$Q_{eff}^{-1} = Q_{int}^{-1} + Q_{scatt}^{-1},$$

where

$$Q_{scatt} = \frac{\omega \Lambda_S}{\beta}.$$

Λ_S is the scattering mean free path for S waves (Fehler et al., 1992). In our model, the shear mean free path value was 411 km at 2.0 Hz in the crust, resulting in a Q_{scat} of 1463 and therefore a Q_{eff} of 845, which agrees well with the estimates of Martynov et al. (1999).

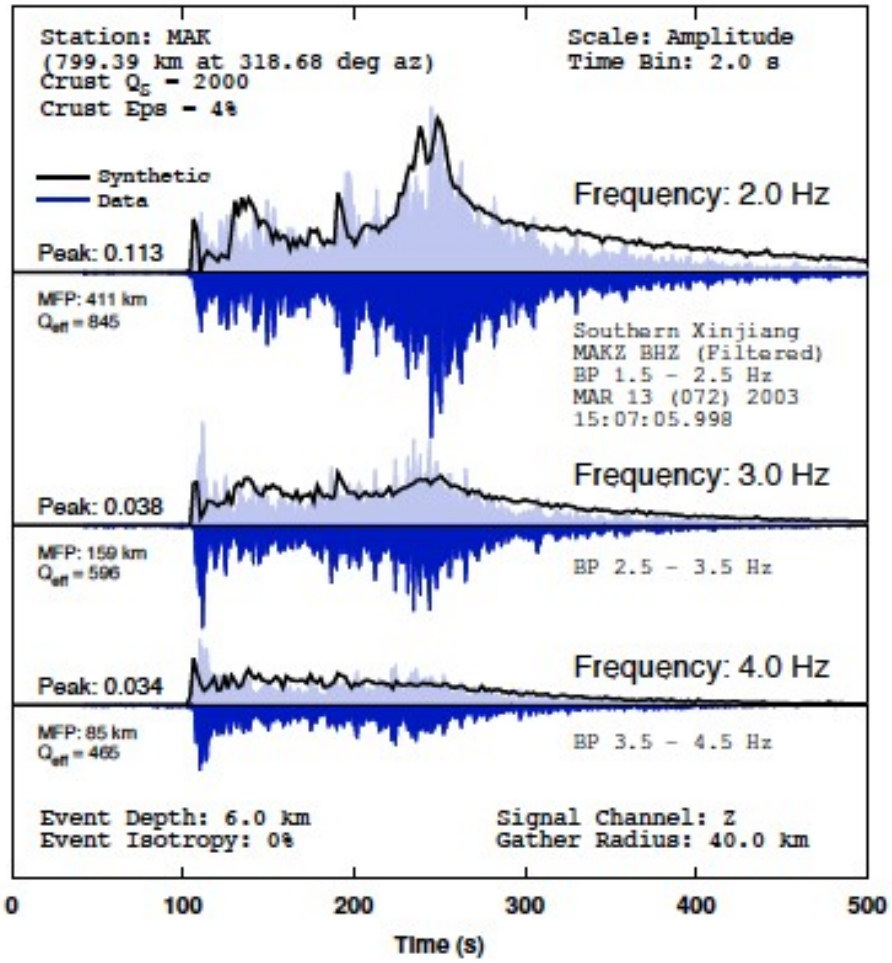

Figure 10. Synthetic and observed waveforms (1-4 Hz) earthquake. *Synthetics compared against data recorded at station MAK for the 2003-03-13 earthquake for frequencies 2, 3, and 4 Hz. Peak amplitudes of the synthetic traces are notated to facilitate comparison between traces. Scattering mean-free paths and effective Q values (combining intrinsic Q and frequency-dependent scattering Q) noted for each trace are for S waves in the crust.*

4.1.7 Observed and modeled explosion with tectonic release

We investigated the effect on high frequency regional phase propagation of explosion sources associated with components of tectonic stress release. These experiments were inspired in part by the work of Bukchin et al., (2001). That study jointly inverted P wave first motions and teleseismic Love and Rayleigh wave spectra for unconstrained moment tensors of earthquakes and nuclear tests in the Lop Nor region. The amount of tectonic release of nuclear tests was expressed as an angle given by the inverse tangent of the ratio of the isotropic to non-isotropic moment tensor components. Our experimental series incorporated moment tensors reported by Bukchin et al. (2001) for the Lop Nor nuclear tests. Envelopes were synthesized for paths to stations MAK and WUS.

For this series of experiments, we used the moment tensor decompositions of several explosion events published by Bukchin et al. (2001) as our starting points. Although they treat the isotropic and deviatoric components as vertically separated, in these runs we treated them as co-located and coherent (meaning a single moment tensor specifies the entire source, as opposed to running the deviatoric and isotropic source radiation events separately and summing the synthetics).

Figure 11 shows an example of one of our event simulations compared to data recorded in several narrow band passed filters for 1 to 4 Hz. We modeled the 1996-06-08 explosion event (mb 5.8) with 30^o, 45^o, and 60^o isotropic angles. We found the best agreement to recorded data at 45^o, representing an equal partition between isotropic and deviatoric moments, supporting the findings of Bukchin et al. (2001) from teleseismic surface waves. Note the explosion with tectonic release strongly enhances Lg at 1 Hz and decreases the Pg/Lg ratio in this frequency band, despite being synthesized at an azimuth that favors Pg based on the deviatoric component of the moment tensor. This suppression of the Pg phase is a result of the isotropic component serving to compensate the tensional principal axis of the composite moment tensor. Although the shift between Lg and Pg amplitude peaks as frequency increases is qualitatively well matched to the recorded data, there is a slight over-representation of the Lg phase, and a marked under-representation of the Pn phase. Further perturbations of velocity gradients beneath the Moho and the model of intrinsic attenuation may improve the fit. We have not, however, yet applied spectral scaling models for earthquakes (Brune, 1970) or explosions (Mueller and Murphy, 1971) to correct for the differences in the shape between radiated P and S waves by the source. Fisk (2006) has documented strong differences between the spectrum of radiated P and S waves in this region. These source spectrum effects will possibly be more important than any additional perturbations to the Earth structure.

We note that our code does not include fundamental mode surface waves and our tests are for relatively long range (>100~km), and high frequency (>1 Hz). At this frequency and range surface waves are usually strongly scattered away by surface topography and near surface heterogeneity. Numerical simulations by Obermann (2013) at ranges on the order of 10 km have found that high frequency surface waves can provide valuable discrimination of source depth and possibly also of tectonic release.

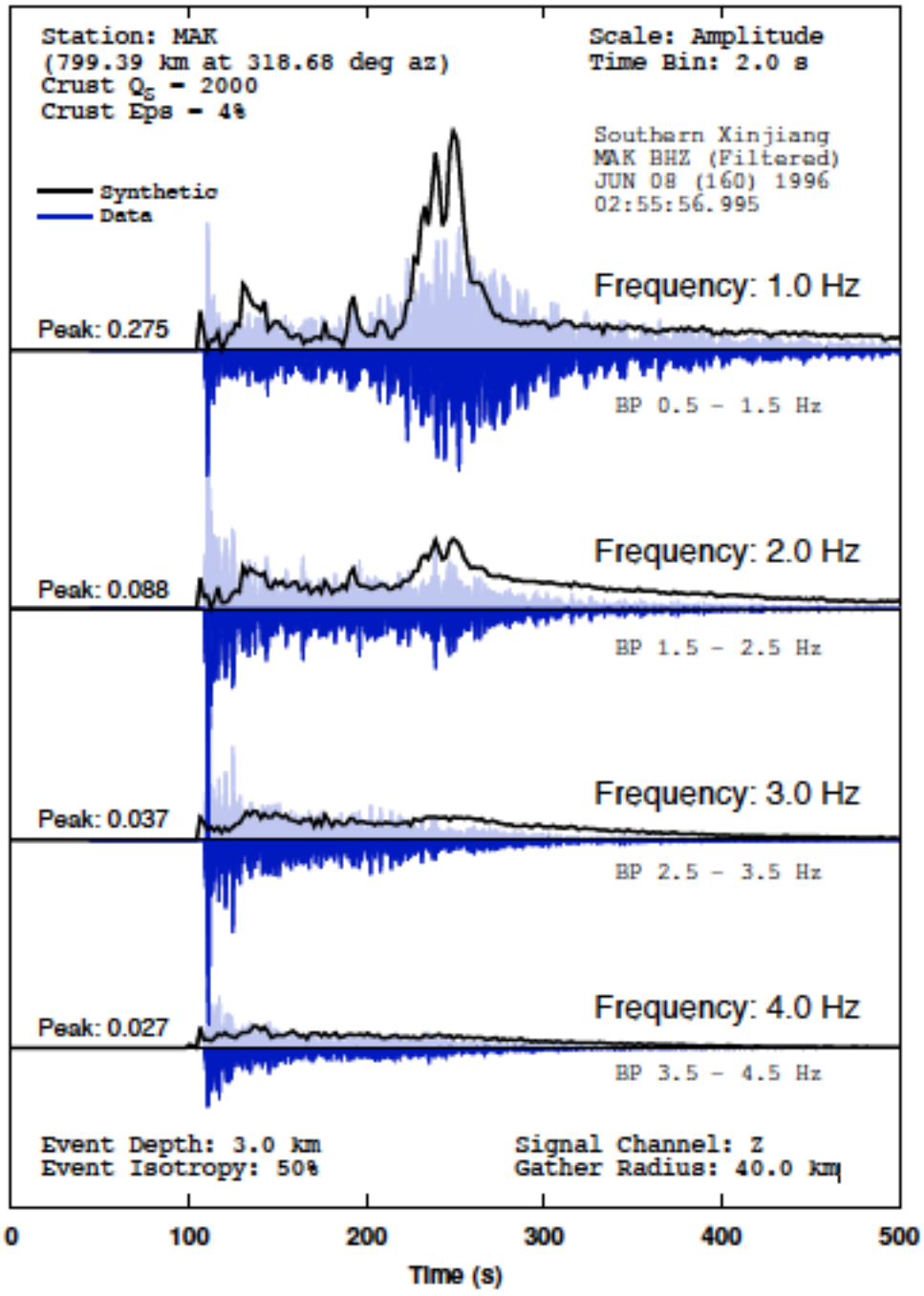

Figure 11. Synthetic and observed waveforms (1-4 Hz) explosion. *Synthetic envelopes for a Lop Nor nuclear test using source mechanism with tectonic release determined from the surface wave study of Bukchin et al. (2001), compared with observed envelopes for the same test. The tectonic release component simulates strike, dip, and rake angles of 280°, 70°,160°. The composite moment tensor models an isotropic angle of 45°, representing an equal contribution from isotropic and deviatoric moments.*

4.2 Regional Phase Blockage by Crustal Structure

The Lg wave is often the largest feature in high-frequency (>2 Hz) seismograms observed at regional (200–1500 km) distance. Lg follows the Sn wave, initially arriving with a typical group velocity of 3.5 km s^{-1} and extends in a complex coda up to 100 s or more. Lg propagation can be represented either by sums of higher mode Love and Rayleigh waves confined to the Earth's crust or by sums of multiple *S* waves critically reflected from the Moho and scattered by small-scale heterogeneities in the crust (Kennett 1986; Keers *et al.*1996). Since *S* waves are not radiated by idealized models of underground explosions, observations of Lg and the amplitude ratio of Lg to regional *P* waves (Pn and Pg) are important to discriminating the seismic signatures of underground nuclear tests from those of natural earthquakes. The efficiency of Lg propagation, measured by the peak amplitude of its coda, can be affected by lateral variations in crustal thickness, scattering and intrinsic attenuation. These propagation effects diminish the consistency of Lg/*P* amplitude ratios to separate earthquake from explosion populations.

Because of its importance to source discrimination, the efficiency of Lg propagation has been extensively investigated, primarily by empirical observation by mapping and contouring path efficiency (e.g. Campillo 1987; Rodgers *et al.*1997; Furumura & Kennett 2001; McNamara & Walter 2001), but also by synthesizing waveforms using analytic, numerical and hybrid numerical/approximate methods applied to well-known and canonical crustal models (e.g. Campillo *et al.*1993; Wu & Wu 2001; Furumura *et al.*2014). General agreement among these studies is that zones of crustal thinning, for example, transitions from continental to oceanic crust, are associated with Lg blockage (Gregersen 1984; Mendi *et al.*1997). The efficiency of Lg propagation across zones of crustal thickening, for example, collisional mountain belts, however,is mixed, often as efficient as propagation across laterally homogeneous regions of continental crust, with blockage controlled by either intrinsic attenuation, scattering or by other large-scale complex structure (McNamara & Walter 2001; Sens-Schönfelder *et al.* (2009). Fig. 12 summarizes these Lg behaviours from a few well-studied paths in Europe and Japan.

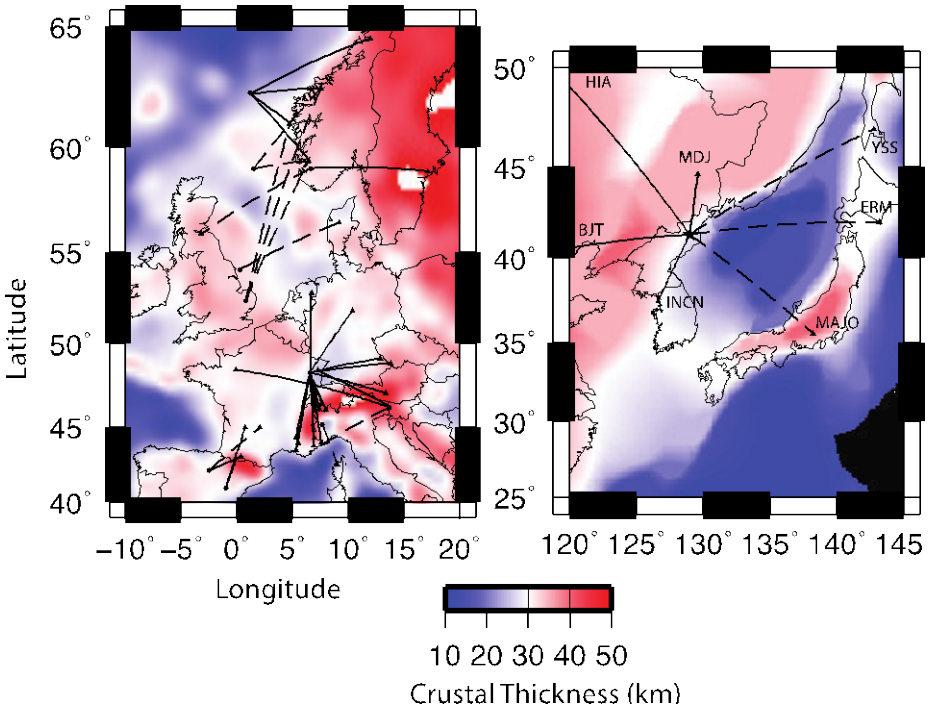

Figure 12. Example efficient *(solid lines)* and inefficient propagation paths of Lg. *In Europe and Japan assembled from Gregersen (1984), Campillo et al. (1993), Chazalon et al. (1993), Shapiro et al. (1996), Mendi et al. (1997), analysis by the authors of FDSN records of an earthquake in France (49.34°N, 6.62°E on 2003 February 22 at 20:41:04) and an analysis of a North Korean earthquake from G. Wagner 2017 (personal communication). Crustal thicknesses are from Grad et al. (2009) and the Cornell Moho (http://atlas.geo.cornell.edu/ctbt/geoid.html).*

Prior computational studies of Lg blockage in crustal thinning models include Maupin (1989), Cao & Muirhead (1993), Vaccari & Gregersen (1998), Zhang & Lay (1995), Mendi *et al.* (1997) and Wu & Wu (2001). The majority of these studies are limited to 2-D propagation and *S* waves polarized as *SH*. A radiative transport study that examined localized heterogeneity as an explanation for Lg blockage for paths crossing the western Pyrenees can be found in Sens-Schönfelder *et al.* (2009). Although 3-D, that study considered a relatively simple crustal model consisting of a layer over a half-space, locally perturbed by a velocity anomaly specified by a rectangular solid. Applying a similar radiative transport algorithm, this paper examines the effects of crustal thickness variations, scattering and intrinsic attenuation on the 3-D propagation of high-frequency Lg and Pg. The modelling is implemented by our Radiative3D code (Sanborn *et al.*2017), which includes the effects of multiple scattering in 3-D, mode conversion (*P* to *S* and *S* to *P*) and polarization changes induced by statistically described small-scale (≤ wavelength) heterogeneity. Our code also includes the effects of source radiation pattern, intrinsic attenuation, reflection/transmission by layered structures, generalized variations in crustal thickness, and the focusing and defocusing by large-scale deterministic structure. Since the North Sea Central Graben has been a well-studied path for Lg blockage investigations, the canonical models for crustal thinning effects are approximately scaled

to the cross-sectional dimensions of the North Sea graben shown in Mendi *et al.* (1997) for a path from Norwich, UK, to station BLS near the Blåsjøreservoir in southern Norway. The dimensions of this structure are also close to those of the oceanic basin of the Ligurian Sea crossed by Lg paths from France to Corsica in the studies by Shapiro *et al.* (1996) and Contrucci *et al.* (2001).

4.2.1 Applying radiative transport

The majority of previous modelling studies utilized 2-D (range and depth) numerical simulations. In order to compare with these prior studies with a 3-D method, we have chosen to make our models azimuthally symmetric, with the crust modification region (pinch or bulge) occupying a constant range from the source. This allows us to look at 2-D cross-sectional views of our model and wave-front snapshots by plotting range and depth only (collapsing out azimuth). The modelling thus simulates the propagation of seismic phases normal to the strike of a modified region, similar to previous 2-D studies, but includes the effects of out-of-plane scattered arrivals.

Another advantage of the azimuthally symmetric model design is that, for a hypothesized strike-slip earthquake source, we can capture and isolate particular propagation modes based on the azimuth selected for a linear array of virtual seismometers. For a strike-slip mechanism the apportionment of radiated energy by polarization mode is a function of azimuth. For example, a seismometer array aligned with either the compressional or tensional principal axes of a strike-slip source will isolate a *P–SV* system of polarized waves, whereas an azimuth intermediate between the compressional and tensional axes will isolate *SH* polarized waves, as these azimuths coincide with the null-planes for *P*-wave radiation. Note, however, that for a strike-slip source, there are no null planes for *S*-wave radiation, and thus it is impossible to completely isolate *P* radiation. For this purpose, however, we can simulate a pure isotropic explosion source. Thus it is possible to produce simulations that illustrate the model effects on Pg in isolation from horizontally polarized Lg, and vice-versa.

The gross structure of our models are fan-shaped to catch outward-radiating wave fronts within an azimuthal span of 90°. This is wide enough to enclose both an expanding *SH* wave front and an expanding *P–SV* system of wave fronts. The radiance maxima of these two systems have a 45° angle between them, so the 90° angular spread of the model means both azimuths of interest are well within the model bounds. We place three linear arrays of virtual seismometers. One array catches *SH*, one catches *P–SV*, and a third is intermediate between them and catches a mixture of all modes. The model extends to a range of 1020 km from the source and to a depth of 360 km below the Earth's surface. A range of 1020 km is large enough that the Earth's curvature can affect timing and amplitudes. As such, we include Earth-like curvature in the design of our model. The general modelling strategy is illustrated in Fig. 13. In all models except the baseline model, the wave fronts must cross a region of crustal variation (RCV), indicated by the brown band in the plan view (Fig. 13: top), and shown as a pinch region in the side profile view (Fig. 13: bottom). We consider RCVs in the form of crustal pinches, bulges

or regions of high scattering due to heterogeneity. The layers of the model follow Earth-like curvature, as can be seen on the side profile.

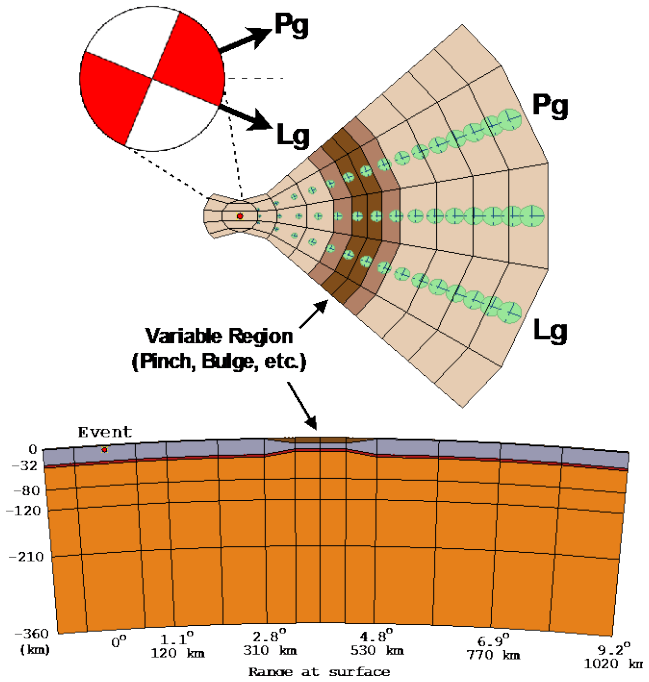

Figure 13. Models and paths relative to radiation pattern to examine Lg and Pg. *Models are fan shaped (plan view, top) to accommodate outward radiating wave fronts within a 90° azimuthal arc from the source, which is indicated by a red dot in the handle of the fan. Choice of source parameters and seismometer arrays (illustrated by green discs representing gather area of every 10th seismometer) allows selective isolation or mixing of Lg and Pg phases. A crust variation region (pinch, bulge or high scatter region) begins at a range of 310 km from the source and concludes at 530 km. The model is azimuthally symmetric so that expanding wave fronts are perpendicularly incident on the structural modification. Model layers follow Earth-like curvature, as shown in the profile view (bottom).*

The event we simulate is alternately an earthquake or an explosion at a depth of 10 km. For the earthquake, we use strike, dip and rake parameters of 22.5°, 90° and 0°, respectively. This is a strike-slip source oriented so that the compressional and tensional principal axes are parallel to the ground and the null axis is oriented vertically. With these parameters, the compressional principal axis extends outwards at an azimuth of 67.5° east of north, which becomes a favoured direction for sampling the Pg phase. Offset 45° from that, at an azimuth of 112.5° east of north, is a maximum for *SH*. This becomes a favoured direction for sampling Lg. The radiation pattern is illustrated in Fig. 14. The strike orientation of the event is chosen to align with the virtual seismometer arrays such that one array catches *SH* polarized energy, which predominantly manifests itself as the Lg phase, and another array catches *P* polarized energy along with a small contribution of *SV*, which predominantly manifests itself as the Pg phase.

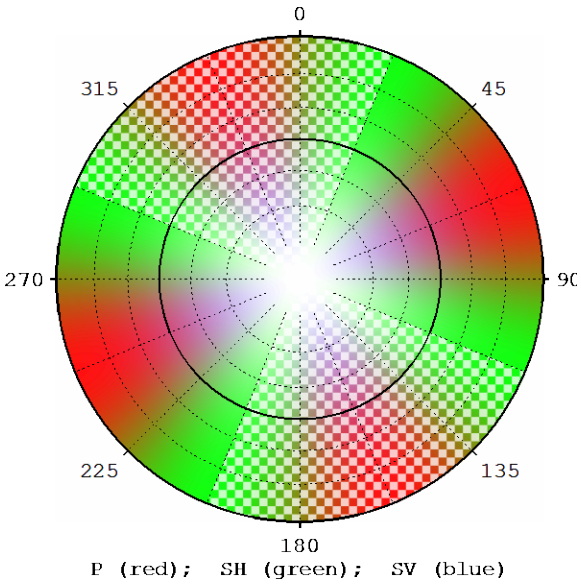

Figure 14. Radiation pattern of simulated earthquake source. *Showing directional dependence of polarization mode (P, SV or SH). The chosen strike-slip focal mechanism isolates SH radiation on azimuths of 22.5°, 112.5°, etc., which we use to situate seismometer arrays to observe Lg effects separate from Pg effects. Similar to classic beach ball diagrams, we plot polarization on the lower half focal sphere, using colour density to indicate composition of polarization mode. Solid colouration indicates outward first motion, whereas checkerboard colouration indicates inward first motion.*

4.2.*2* Models for blockage experiments

For the purposes of investigating different crust and bulge structures, we enumerate a set of model identifiers based on the labelling pattern NSCP *nn*, where *nn* is a numeric code, and the identifier can be read as North Sea Crust Pinch model, variant *nn*. (The model dimensions and positioning of the structural variations are loosely based on a path crossing the North Sea Central Graben.) We use NSCP 00 to refer to an unpinched, flat crust model, which can serve as a baseline to observe effects of pinches and bulges, which we will label with numeric codes 01 and above. The models are illustrated in Fig. 15 and layer thicknesses and attributes are tabulated in Tables 2 4.

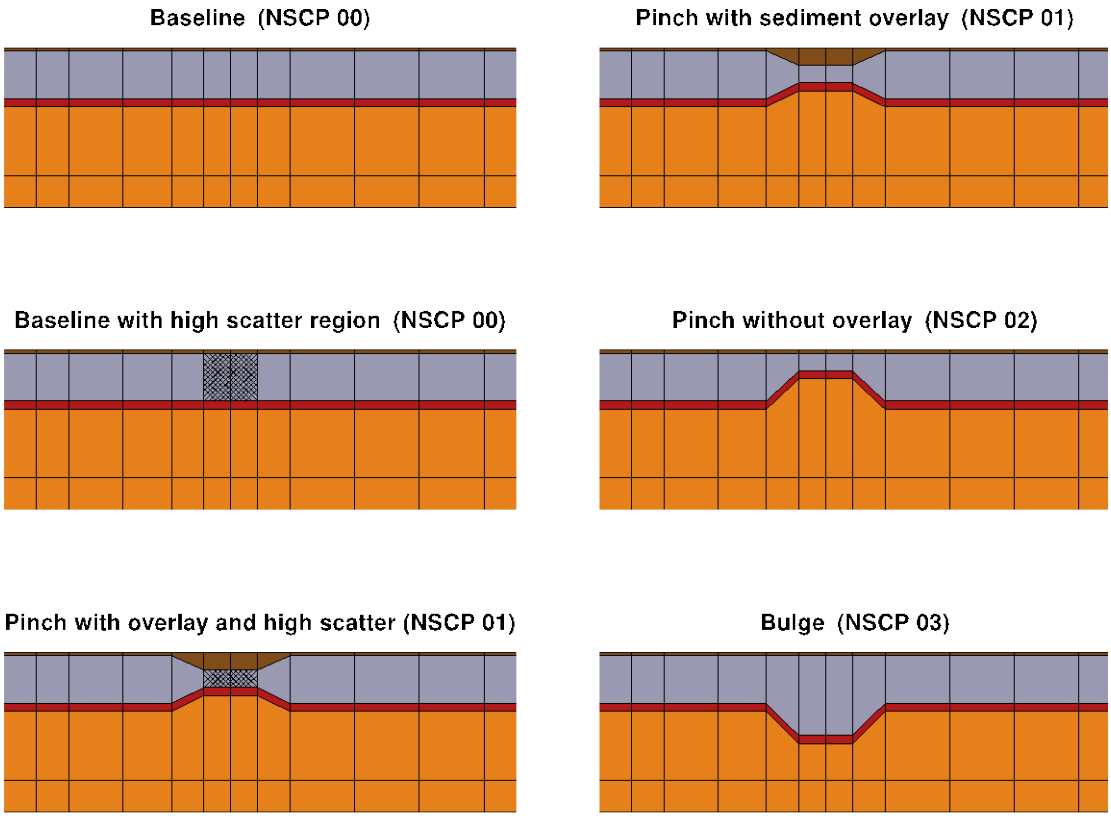

Figure 15. Profiles of crustal thickness variations for variants of the North Sea Crust Pinch (NSCP) model series. *Four models perturb the layer structure within a localized region (pinches and bulges), and two add a localized high-scattering region in the crust layer. Each model is divided into four major structural layers: a low-velocity sediment layer; a crust layer; a thin (5 km) high-gradient Moho transition layer; and the mantle, extending to a bottom of 360 km. The layers support velocity gradients, and reflection and transmission are simulated (including mode conversion) at layer interfaces due to velocity discontinuities.*

Table 2. Layer thicknesses in pinched/bulged regions of the NSCP models.

	NSCP 00	NSCP 01	NSCP 02	NSCP 03
Sediments	2 km	11 km	2 km	2 km
Crust	30 km	11 km	11 km	50 km
Moho transition	5 km	5 km	5 km	5 km
Mantle upwell	0 km	10 km	19 km	−20 km

NSCP 00 is the baseline condition in which the variation region is unchanged from the remainder of the model. For mantle upwell, negative values imply a model in which the Moho descends into the mantle, as in a mountain root or crust 'bulge'.

Table 3.Velocities (km s−1) and densities (gm cm−3) for each layer in NSCP models.

	Density	*P* wave speed	S wave speed
Sediments	2.20	4.50 to 4.52	2.60 to 2.61
Crust	2.80	6.20 to 6.24	3.58 to 3.60
Moho transition	3.39	7.70 to 8.00	4.44 to 4.46
Mantle	3.40	8.0 and up	4.46 and up

Ranges imply a gradient from top to bottom of layer.

Table 4. Heterogeneity parameters and scattering statistics in model layers.

	ν	ε	*a*	κ	MFP$_P$	MFP$_S$	$\Lambda_P^{(absorb)}$	$\Lambda_S^{(absorb)}$
Sediments	0.8	1 per cent	0.2 km	0.2	8932 km	4632 km	161 km	41 km
Crust (baseline)	0.8	1 per cent	0.2 km	0.3	13669 km	6802 km	1665 km	427 km
Crust (enhanced scattering)	0.8	10 per cent	0.2 km	0.3	137 km	68 km	1665 km	427 km
Moho transition	0.8	1 per cent	0.2 km	0.4	18774 km	8979 km	2073 km	530 km
Upper mantle	0.8	1 per cent	0.2 km	0.5	16128 km	7364 km	1383 km	319 km
(continued)	$Q_P^{(scat.)}$	$Q_S^{(scat.)}$	$Q_P^{(int.)}$	$Q_S^{(int.)}$	DP$_P$	DP$_S$		
Sediments	24943	22390	449	200	−0.087	0.180		
Crust (baseline)	27704	23877	3374	1500	−0.186	0.060		
Crust (enhanced scattering)	277	239	3374	1500	−0.186	0.060		
Moho transition	30640	25412	3384	1500	−0.236	−0.007		
Upper mantle	25334	20748	2172	900	−0.238	0.007		

Weak scattering is simulated throughout the model, but a few test conditions call for enhanced scattering within the zone of crust variation (the pinch/bulge/scatter region). Parameters ν, ε, *a*, and κ (defined in the text) describe the von-Kármán heterogeneity spectrum of the medium. Mean free paths for *P* and *S* scattering at 2.0 Hz are shown and compared with the absorption lengths of intrinsic attenuation. An effective 'scattering *Q*' is computed from the mean free paths and compared with intrinsic *Q*'s. Scattering directionality is summarized by mean cosine of scattering angle, which we refer to as 'dipole projection' or DP. Absorption lengths $\Lambda_{P,S}$ are calculated from intrinsic attenuation $Q_{P,S}^{(int)}$, velocity $V_{P,S}$, and radian frequency ω of the simulated wave by $\Lambda_{P,S} = V_{P,S} Q_{P,S}^{(int)} / \omega$.

All model variants consist of seven structural layers. These are a sediment layer, a layer representing the solid bulk of the crust, a thin Moho transition layer, and four layers spanning the upper mantle down to a depth of 360 km. The four mantle layers follow AK-135 (Kennett *et al.*1995), and the three crust layers are loosely patterned after the crustal structure in the North Sea region. A velocity gradient in each layer is prescribed, such that velocity increases with depth, starting from some initial value, and ending at a final value, which may or may not be continuous with the next layer. Interlayer velocity discontinuities are utilized between the sediments and the crustal layer and between the lower crustal layer and the Moho transition layer. As in AK-135, a discontinuity is included at 80 km depth.

All layers simulate scattering effects appropriate for a von Kármán heterogeneity spectrum. We utilize a fractional fluctuation ε of 1 per cent in local *P* and *S* velocities and a spectrum scale length corner *a* of 0.2 km in all layers to provide a weak background level of scattering throughout the model. The scattering formulation is that of Sato *et al.* (2012) and we specify also the density fluctuation $\Delta\rho/\rho = \nu\,\Delta V_P/V_P$ as a fraction ν of the *P* velocity fluctuation, as well as the Hurst parameter κ which controls rate of decay below the corner scale length. Scattering is simulated as a stochastic process controlled by angular probability distributions precomputed for each model cell. These distributions are dependent on the local average background velocities, and in layers with velocity gradients, the scattering behavior is uniform throughout the layer and assumes the background velocity as specified at the top of the layer. Some models additionally feature a localized increase in the heterogeneity to 10 per cent fractional velocity fluctuation in the crust elements located within the structural variability region. Heterogeneity parameters and scattering statistics are tabulated in Table 3.

4.2.2.1 NSCP 01: Graben zone with sedimentary overlay

Model variant NSCP 01 includes a pinched region with a sedimentary overlay and a slight mantle upwelling. In the pinch region, the lower crust layer tapers from an initial thickness of 30 km down to a final thickness of 11 km. The tapering is coupled with a broadening of the sediment layer from its initial thickness of 2 km to a final thickness of 11 km, and an upwelling of the mantle layer of 10 km. (The Moho transition layer thickness is unchanged; however the layer migrates upwards to remain intermediate between the ocean basalt and mantle layers.) In this configuration, the surface elevation remains fixed throughout the pinch region. The width of the fully pinched region is 100 km, and is bracketed on either side by taper regions of 60 km each, such that the complete width of the crust variation region is 220 km. The variation region begins at a range of 310 km from the source and concludes at 530 km. No changes are made to the velocities in variation region, only to the layer thicknesses. (The velocity gradients, however, are enhanced or diminished with the narrowing or broadening of the layers, so as to preserve the velocity values at the layer boundaries.)

4.2.2.2 NSCP 02: Thin crust due to mantle upwelling

Model variant NSCP 02 includes a similar pinch structure to NSCP 01 (lower crust tapering from 30 km down to 11 km). This model, however, does not include a sedimentary overlay. (The sediment layer remains at a constant thickness of 2 km throughout the model.) Instead, the mantle upwelling is increased to 19 km. As in NSCP 01, the surface elevation remains unchanged throughout the variation region.

4.2.2.3 NSCP 03: Crust bulge protruding into mantle

NSCP 03 is a crust bulge model. As in NSCP 01 and NSCP 02, we do not modify the elevation of the model surface, but instead allow the crust to bulge into the mantle. In the variation region, we thicken the crust from its initial thickness of 30 km to a final thickness of 50 km. Keeping the sediments thickness, Moho transition thickness, and surface elevation unchanged, this translates to a 20 km intrusion into the mantle. As in models NSCP 01 and NSCP 02, the variation region begins at 310 km and spans 220 km, which includes 100 km fully bulged span bracketed on either side by 60 km taperregions.

4.2.2.4 Models featuring scattering zones

For each model structure, we additionally simulate a case where the heterogeneity in the region of crust variation (from 370 to 470 km, corresponding to the fully pinched or fully bulged regions) is increased from 1 per cent to 10 per cent fractional velocity fluctuation. In the case of structural baseline NSCP 00, in which there are no changes in layer thickness in the crust variation region, the enhanced scattering variation tests the effects of a high-scatter zone separate from the effects of structural variation. There is no additional heterogeneity (above the 1 per cent background levels present throughout the model) in the regions that correspond to the taper zones of the pinch/bulge models. The scattering zones are indicated by hatch markings in Fig. 4, and the heterogeneity parameters are listed in Table 3.

4.2.3 Lg and Pg blockage experiments

The simulation outputs primarily take the form of traveltime curves and energy curves. Both are representations of the signals collected by single-azimuth linear arrays of virtual seismometers, thus giving information about the wave fronts propagating along those azimuths.

The traveltime curves are plots of energy amplitude observed at the surface as a function of range and time. Visual inspection of these plots allows easy identification of individual seismic phases and their relative strengths and temporal profiles.

The energy curves illustrate time-integrated total energy recorded by the receivers as a function of range from the source. In this sense, they correspond to integrating the time axis on the traveltime plots, while retaining the range axis. As with the traveltime plots, these plots represent signal along a single azimuth as recorded by a single virtual

seismometer array. The energy curves are one way to illustrate and quantify the effects of model structure on the outward propagating wave fronts. Towards this end, they are most useful when used with arrays that isolate a single seismic phase, such as Pg or Lg, as it enables us to observe the effects on those phases individually.

4.2.3.1 Wave-front time-series

The time-series plot in Fig. 16 shows profile views (range and depth) of energy packets (hereafter referred to as phonons) propagating through model NSCP 01 as a function of time. This gives an indication of the bulk propagation characteristics of the wave-front propagation, and provides some context for interpreting the more quantitative traveltime and energy curves. In the figure, blue dots represent *S*-polarized phonons and red dots represent *P*-polarized phonons. The temporal snapshots are selected still frames from an animation that can be viewed by downloading files supplied in a supplement.

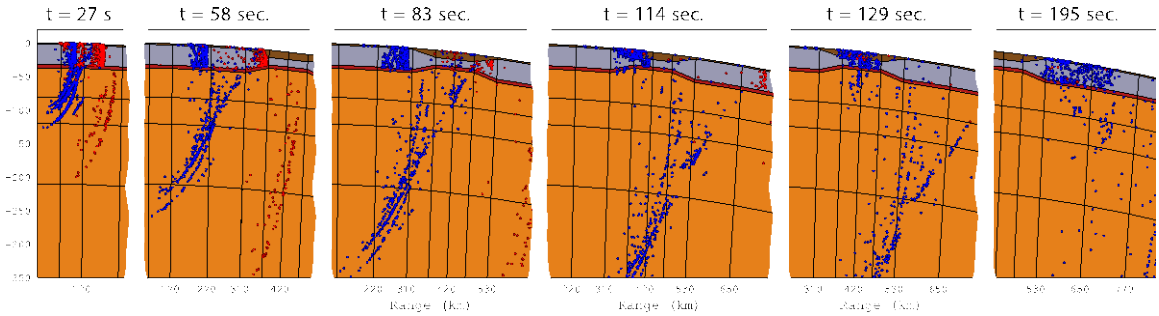

Figure 16. Earthquake time-series in crustal pinch model (NSCP 01). *The time-series shows phonon propagation through a crust pinch earth model and illustrates how wave fronts evolve with time. Red markers represent P-phonons and blue markers represent S-phonons.*

4.2.3.2 Traveltime curves

Traveltime curves are presented in Figs 17–19 and indicate received energy flux as a function of range and time. Plotted image density is proportional to the square-root of the energy flux signal so that the visual presentation is amplitude-like, which better reveals coda detail to the eye. The energies are also scaled by a distance-dependent reference curve determined by a power-law fit to a reference model. The reference curve serves to normalize the image intensity so that phase structure remains easily visible despite range based decay, and in essence corresponds to the removal of the attenuating effects of geometric spreading and intrinsic attenuation. In fact, the decay constant of the reference curve can serve as an empirical measure of the combined effects of these attenuation mechanisms, and in this capacity is most useful in the baseline case where these mechanisms are laterally invariant. The reference curve also helps to highlight how one test case deviates from another. For example, in Fig. 17, the baseline (non-pinched, non-scattering) test case serves as the reference model both for itself and for the pinch model, so that the attenuation posterior to the pinch zone is made plainly visible in the pinch

model by the clear reduction in image intensity. By contrast, in Figs 18 and 19, each model serves as its own reference, which enhances visibility of the detailed phase structure at long range, even though it makes the attenuation with respect to the baseline model less obvious.

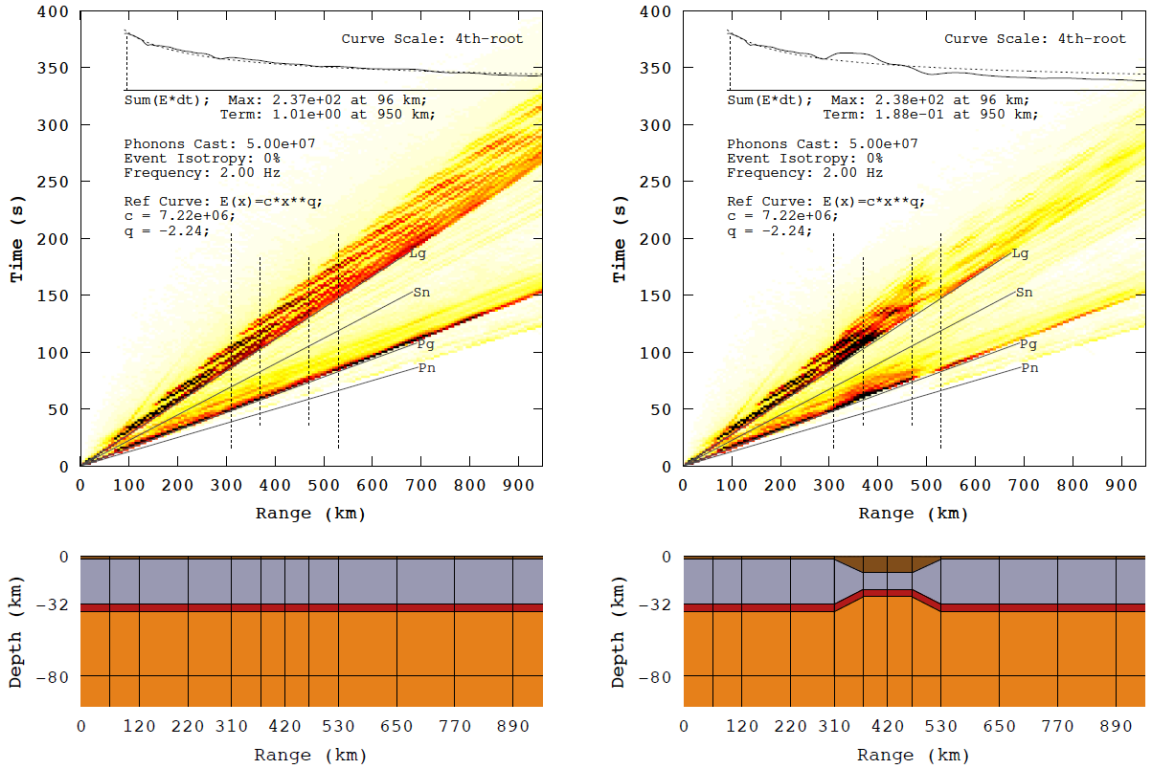

Figure 17. Traveltime curves for the baseline model *(left)* and a crustal pinch model *(right). Showing disruption and attenuation of major phases resulting from crustal structure. Colour density indicates all-component energy amplitude (square root of energy flux across all channels) relative to a distance-dependent reference curve computed by power-law best fit to the time-integrated energy of the baseline model. The common reference curve (dashed line) and time-integrated energy signal (solid line) of each condition are inset at the top of the traveltime curves on a 4th-root scale to accommodate compressed vertical space. The region of crustal thickness variation is outlined by dashed vertical lines, and major regional phase velocities are indicated via velocity slope lines. Source event is an ideal strike-slip earthquake and the array azimuth is intermediate between the preferred azimuths for SH and P–SV radiation, such that Pg and Lg phases are both well represented in the images.*

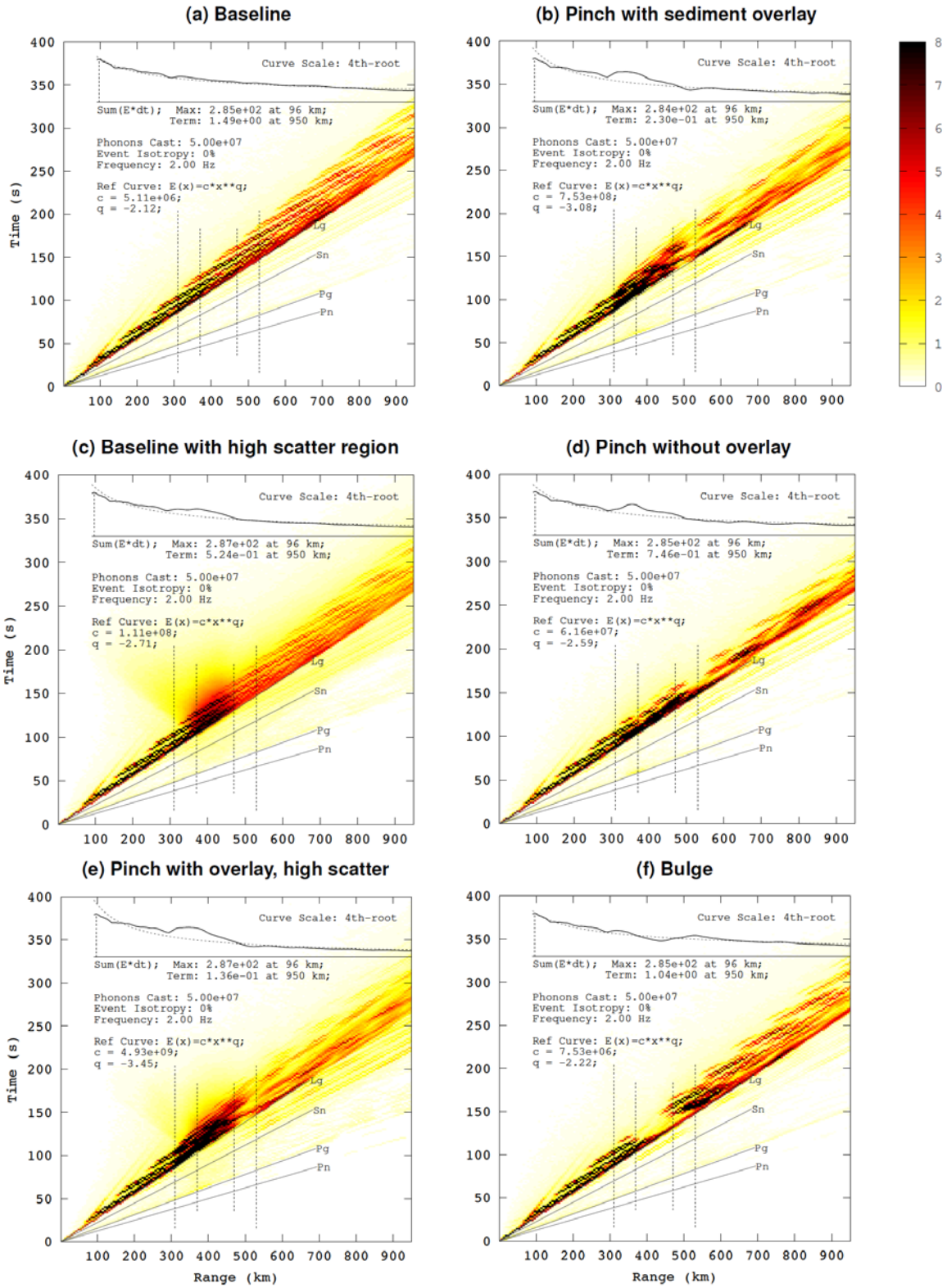

Figure 18. Crustal thickness and heterogeneity effects on all-component energy originating from Lg phase in a variety of Earth structures (*cf*. Fig. 15). *Source is a hypothetical strike-slip earthquake, and energy signal is measured along an azimuth aligned with pure SH radiance. Image density is proportional energy amplitude (square root of energy signal) relative to a reference curve specific to each plot established by a power-law best-fit to the time integrated energy as a function of distance.*

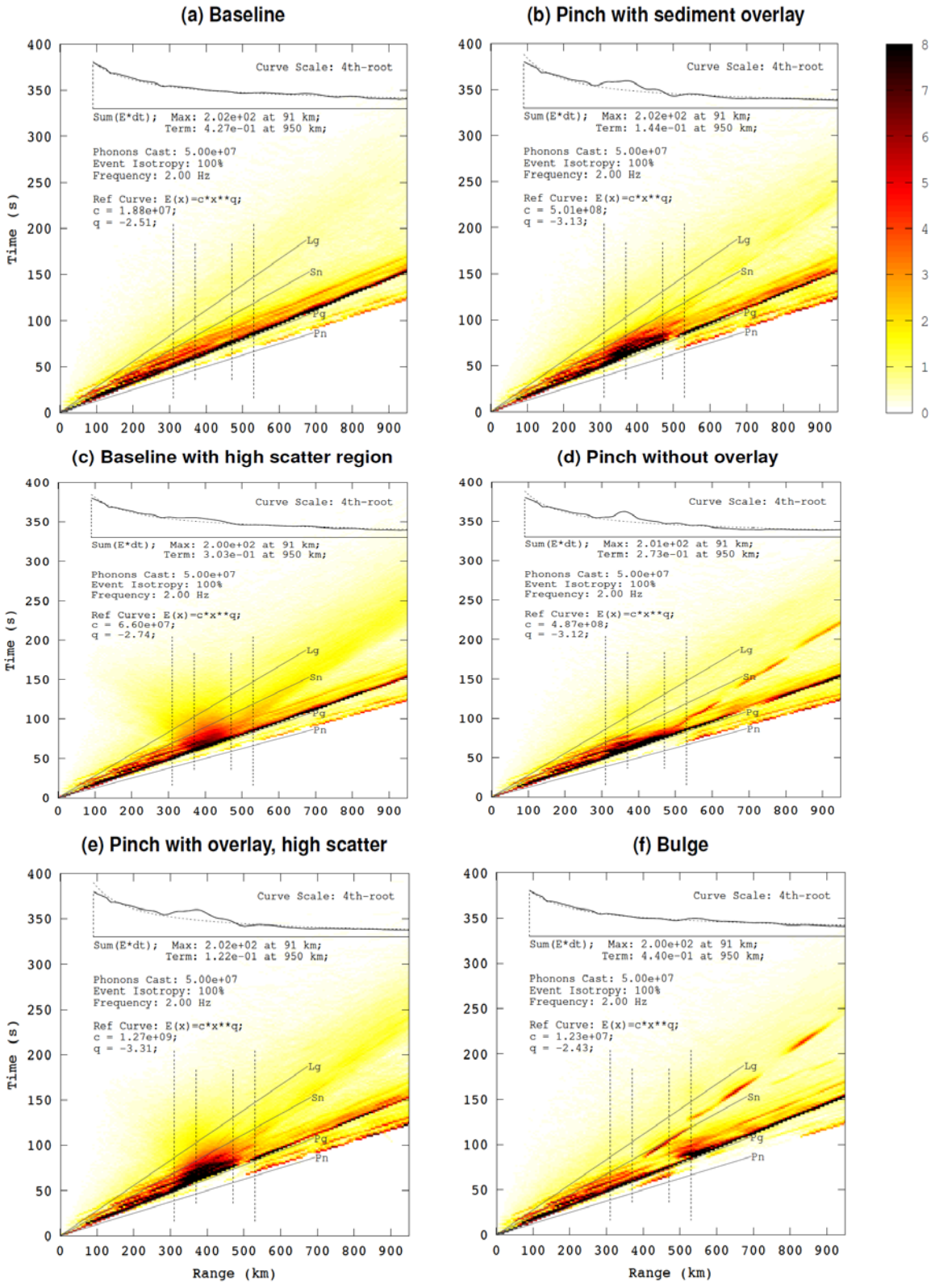

Figure 19. Crustal thickness and heterogeneity effects on all-component energy originating from Pg phase in a variety of Earth structures *(cf. Fig. 15)*. *Source is an isotropic explosion. Image density is a proportional energy amplitude (square root of energy signal) relative to a reference curve specific to each plot established by a power-law best fit to the time integrated energy as a function of distance.*

The energies we display in these plots are summations of all three components of motion, rather than restricting to a single component. This prevents the masking of converted phases which may otherwise fail to appear if they excite a different component of motion. Additionally, since our simulation reports energy flux, which is not identical with squared particle velocity without application of a free-surface correction (a planned but not-yet-implemented software feature), comparison of single-component signal to real data can be non-intuitive. In our experience the channel-summed energy provides more interpretive insight.

Within each traveltime plot, the reference curve used for normalization and the time-integrated energy of the current plot are shown as dashed lines and solid lines, respectively, as an overlay plot. A fourth-root scale is used for this to fit narrow vertical space. Vertical lines outline the crustal variation region. Major regional phase velocities are indicated via velocity slope lines. In the example shown in Fig. 6, array azimuth is intermediate between the preferred azimuths for *SH* and *P–SV* radiation, such that Pg and Lg phases are both well represented in the images. Here we show only the baseline case and the pinch with sedimentary overlay case. Subsequent figures show the full set of test cases along azimuths selected to isolate Pg and Lg phases to facilitate separate analysis of Pg and Lg effects.

The time-integrated energy curves for each model condition are shown on a logarithmic scale in Fig. 20, with separate plots for Lg and Pg effects, and facilitate a comparative analysis of the range-dependent decay of each model structure. These time-integrated energy curves are unwindowed about their respective phases, and thereby include energy from phases that convert from the incident Pg or Lg phase. Note however that the curves for one phase do not include cross-effects from the curve for the other phase, as the azimuthal isolation is sufficient to preclude this. Thus, the energy curves remain a good characterization of energy that *began* as either Pg or Lg.

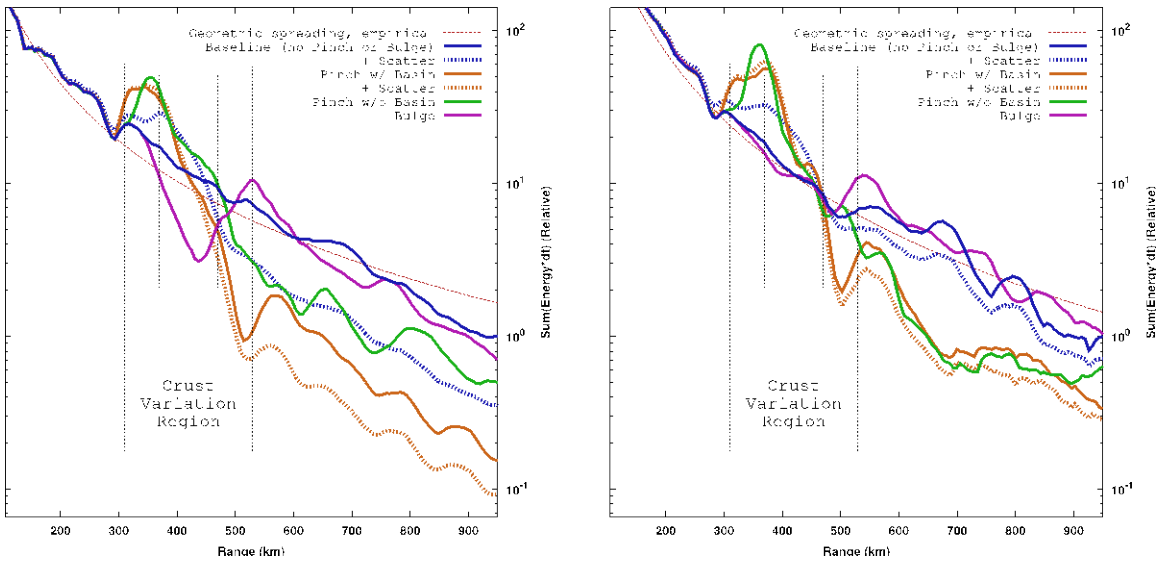

Figure 20. Energy decay curves of Lg phase *(left)* and Pg phase *(right)* by crust structure variation. *Shown here are whole-recording (unwindowed) time-integrated energies as a function of range from source. Lg phase is selected via choice of azimuth from an ideal strike-slip source. Pg phase is selected by use of a pure isotropic source. Unwindowed energies retain the contribution from signal diverted from originating phase into converted phases (e.g. Pn), which can be understood by reference to Figs 7 and 8. Crust structures investigated include: a flat-crust baseline; two structures that include crust pinch regions; and one that includes a crust bulge protruding into the mantle. A further variation on two crust profiles in which the variable region includes enhanced scattering via an increase in fractional velocity fluctuation from* $\varepsilon = 1\%$ *to* $\varepsilon = 10\%$ *are also presented. The red dashed lines show power-law best fits to the baseline conditions and afford an empirical measure of the effect of geometric spreading (albeit not isolated from effects of intrinsic attenuation) on energy. The curves fit energy to* $E(r) \propto r^{-q}$ *with* $q = 2.12$ *in the Lg case and* $q = 2.51$ *in the Pg case.*

4.2.3.3 Pinch versus Scattering Effects on Lg

Here we examine the results from models NSCP 00 with scattering and NSCP 01 without scattering and compare and contrast the ways in which they differ from the baseline model. The two types of crust variation being considered here are a zone of high scattering and a zone of pinched crust with an overlaid sedimentary basin. In the next subsection, we compare the two pinch models (with and without sedimentary overlays) and the bulge model against each other.

First, consider Figs 18(a)–(c). These show the traveltime plots along the azimuth favouring *SH*-polarized Lg for the baseline model (a), the pinch with sedimentary overlay model (b), and scattering-region model (c). This enables us to investigate the differing ways in which the crust pinch and scattering region disrupt the travel of the Lg phase through the variation region.

Both test cases (b) and (c) are associated with a reduction of energy at long range compared with the baseline case (a). This reduction can be made quantitative by inspecting the energy curve comparison in the left panel of Fig. 20, which shows the time-integrated energy curves (surface energy flux as a function of distance from source event) for a selection of model conditions recorded along the Lg azimuth. In that figure, along with the quantitative summary in Table 5, we can see that case (b) (pinch with basin) resulted in an energy reduction of approximately −8 dB at the terminal distance of 950 km. Similarly case (c) (baseline plus scattering) was associated with a reduction of approximately −4.5 dB at the same distance. The greatest attenuation was achieved by the mixed pinch and scatter condition, a reduction of approximately −10.4 dB, showing the more-or-less additive quality of the two attenuation mechanisms. Terminal range attenuations are tabulated in Table 5.

Table 5. Energy attenuation with respect to baseline of Lg and Pg phases at 950 km from source (420 km beyond conclusion of crust variability region), as summarized from Fig. 9.

	Lg	Pg
Baseline (NSCP 00)	0 dB	0 dB
+ Scatter (NSCP 00)	−4.53 dB	−1.49 dB
Pinch with Basin (NSCP 01)	−8.11 dB	−4.73 dB
+ Scatter (NSCP 01)	−10.38 dB	−5.44 dB
Pinch without Basin (NSCP 02)	−2.99 dB	−1.94 dB
Bulge (NSCP 03)	−1.54 dB	+0.13 dB

Energies are whole-recording (un-windowed) time-integrated three-component energies, and thus include contribution from converted phases and scattered energy resulting from interaction of the originating phase (Pg or Lg) with the model structure.

Although both the scattering region and the pinch-with-overlay test conditions resulted in significant attenuation on the far side of the variation region, there is a difference in the qualitative character of the attenuation, as can be seen again in the traveltime plots of Fig. 18. First, observe that in the baseline condition, the Lg phase is actually a superposition of many contributing multiple SmS paths as a result of the crust layer acting as an effective waveguide. This is seen in the plot as a striated grouping of many

parallel phase curves propagating as a wave train within a broad velocity window surrounding the nominal Lg phase velocity. The banding structure is very cleanly visible in our simulated baseline traveltime plot due to several factors: (1) the relatively weak background heterogeneity spectrum of the bulk model, which makes the layers of our model a very clean propagation medium, in contrast to real Earth structure characterized by a rich spectrum of small-scale heterogeneity, (2) the idealizations of the ray-theory method of propagation at the heart of the radiative transport method, which does not simulate diffraction effects that might serve to wash out or blur the banding structure in real Earth propagation and (3) the precise regularity of the idealized, simplified and uniform layer structure of our model, which preserves the coherence of many multipaths due to the lack of fine lateral variations in the thicknesses of the layers or the bulk and shear moduli of the media. The result is an artificially clean-looking Lg wave train in the baseline traveltime plot. These plots, however, become useful in differentiating the disruption mechanisms of pinch versus scattering variation regions.

In particular, we note in the scattering case that the energy amplitude is significantly attenuated, but that the multipath structure of the wave train and the width of the velocity window in which it arrives are largely unaffected. The scattering seems to result merely in a reduction of energy reaching the far side of the variation region, with little change in the character of the arriving signal. The mechanism of action here is almost certainly simple deflection of energy. The traveltime plot would seem to indicate a measurable degree of lateral scattering and back-scattering, as indicated by two distinct graphical features, to be described in what follows. Lateral scattering would include a deflection of the propagating phonons either left or right (w.r.t their propagation direction) or up-or-down. As we are probing an *SH*-polarized Lg phase, we would expect the left-right scattering to dominate, although an up-down fraction would exist to a lesser extent. In either case, both are loss mechanisms. The left-right scattering will divert energy away from the probed azimuth, which represented one of the four amplitude magnitude directional maxima in the *SH* radiation pattern, and into the Pg azimuths where *SH* radiation is at a minimum. Thus, more energy should be scattered away from this azimuth than into this azimuth, and the result will be an overall attenuation. The fraction of phonons that get scattered into up or down directions, on the other hand, will be lost due to other mechanisms. Those trending downwards may make it into the mantle, and thus be lost. Those trending upwards will reflect off the surface, and will then trend downwards. In the latter case, though, they will have interacted with the surface, and this should be visible. Indeed, in the distance range of about 340 km to about 460 km of Fig. 18(c), the Lg phase manifests a visible halo, appearing as orange in the colour scale used in the plot. We believe this may be the result of phonons being scattered into the surface before being reflected downwards and being lost. The second visible feature in the travel time plot is a reflected phase originating at the onset of the scattering region at 370 km, and extending backwards with an Lg-like retrograde velocity in the time window between 120 and 200 s. The feature appears yellow on the plot and is faint, but visible. We believe that this represents back scattering.

The mechanisms are different for condition (b) (pinch-with-overlay), however. In this condition, no abnormally high scattering is occurring in the crust variation region. In

contrast to condition (a), wherein the phase structure is attenuated but not significantly disrupted, in condition (b) the banded multipath structure of the signal is severely disrupted in the variation region, and does not survive as a clear multipath signal on the far side of the region. There is still a clear Lg phase, and the timing of the phase is similar (the energy still falls within a very similar velocity window), but the signal has become amorphous in character. This must be a result of a perturbation of the waveguide character of the crust layer in the crust variation region.

We can get some clue as to what is happening by again looking at the energy curves in the left panel of Fig. 20. The pinch-with-overlay condition is represented by the solid orange line, and the baseline condition by the solid blue line. The blue line follows a more-or-less uniform trend of decaying energy with increasing distance, as would be expected. The pinch line, however, experiences a major downward shift within the variation region and resumes a more gradual decaying trend after the region. An interesting aspect of the trend inside the variation region is that it begins with an initial increase in the energy interacting with the surface that starts slightly anterior to the onset of tapering leading to the pinch region, reaches a maximum as the tapering approaches the fully pinched region, then trends sharply downwards throughout the pinched region, and finally recovers some energy in a narrow region near the conclusion of crustal re-broadening and the region immediately posterior to the variation region. These three phenomena need explaining: the sharp decline of energy within the variation region, the initial amplification of energy, and the final amplification (recovery) of energy. Some possible explanations are suggested here, and in the next subsection we will attempt to corroborate them by investigating different pinch and bulge structures.

The sharp decline of energy in the pinch region is most likely the result of phonon ray paths that transmit into the 11 km thick sedimentary basin overlaying the pinch region, wherein they become trapped until they exit back into the crust on the posterior side of the variation region. The sediments layer is a low-velocity, high intrinsic attenuation (high Q^{-1}) zone, with also a shortened scattering mean free path (compared to the crust layer in the baseline model). As such, the energy content of each phonon will decay much more rapidly in the sediments layer than in the rest of the model. Because of the sharp velocity discontinuity between the sediments layer and the crust layer, down-trending phonons are very likely to reflect upwards, and multiple reflections between the surface and sediment-crust boundary mean that the sedimentary basin will be a waveguide for a slowly moving, multiply reflected, highly attenuating, Lg-like phase that will separate from the faster moving Lg phase still propagating through the narrowed crust. Another loss mechanism would be phonons that transmit from the crust layer into the mantle as a result of the reduced angle-of-incidence (which would tend to increase the transmission coefficient) that would occur where the crust floor angles upwards to produce the tapering region.

The initial upswing in energy in the anterior tapering region is harder to explain, though two possible mechanisms may play a role. One is that the upward grading of the crust floor in the anterior tapering zone would bend rays reflecting off of it from a more glancing to a more directly upward trajectory towards the surface. Furthermore, as the ray

transmits from the crust to the sediments layer, there is a decrease in velocity that would bend the ray towards the interface normal, which would be an additional adjustment towards vertically upwards propagation. These two bending events would have the effect of focusing the energy towards the surface, and might be enough to substantially increase the energy flux rate at the surface in that narrow region, before the attenuating effects of the sedimentary layer begin to dominate. The fact that the increase begins about 10 km prior to the onset of the tapering zone is puzzling, but may actually be a measurement artefact rather than a physical effect, as the virtual seismometers at 300 km range have a gather radius of 14 km, and thus are, in fact, sensitive to the leading edge of the crust variation region. Another mechanism that may explain the initial energy upswing is the possibility of rapid multiple reflections between the surface and sharp velocity discontinuity between the sediments layer and the crust layer, in the tapering zone where the sediments layer is still thin enough that the attenuation affect has not yet taken over. In essence, the energy might be rattling around in the sedimentary basin layer, serving to amplify the surface signal in the anterior regions, but ultimately succumbing to intrinsic attenuation as the sedimentary Lg fraction propagates towards the posterior region of the basin.

The energy recovery that happens at the very end of the crust variation region (upswing in the pinch-with-basin series centred at about 540 km in Fig. 20, left panel) is perhaps the hardest to explain, and what is offered here is very conjectural. Again, two specific mechanisms are proposed. First, the rate of multiple reflections, or rattling, that occurs in the basin-shaped sedimentary layer, would increase as the sedimentary Lg fraction reached the tail end of the basin, due to the thinning of the layer back to its nominal thickness. This would increase the interaction of the phase with the surface, and is essentially the same mechanism as is proposed as a partial explanation of the upswing at the beginning of the basin. This effect would be observed in the region slightly before the conclusion of the crust variation region. It should not, however, contribute significantly beyond the conclusion of the region (at 530 km). The second mechanism may explain the remainder of the upswing, which occurs mostly beyond the conclusion of the variation region. Within the pinched-crust region, the Lg phase has separated into a slower-moving sedimentary Lg phase, trapped in the basin and the faster moving crustal Lg, where the thinned crust is still acting like a waveguide at depth. The energy trapped in this waveguide is not interacting with the surface. When the crust re-broadens, however, the energy expands back into the full-width crust and regains the ability to interact with the surface in the same way as it did prior to the crust variation region. So in this sense, it may be that the at-depth crustal Lg, which is shielded from the surface while trapped in the pinch, is returned to the surface after the pinch, and this could be recorded as an increase in surface energy flux in the region posterior to the crust variation region. In fact, a possible visible indicator of this can be seen in the traveltime Fig. 7(b) as an energy-dense temporally sharp pulse almost exactly aligned with the Lg velocity line that is present between 530 km and 680 km.

4.2.3.4 Pinch models compared

To further explain the phenomenology of the pinch-with-overlay model, it is helpful to compare against other models of crustal thickness variation which differ structurally from the pinch-with-overlay model. To that end, we here compare models NSCP 01, NSCP 02 and NSCP 03, which are, respectively, (1) the pinch-with-overlay model, (2) a pinch model with the same degree of crustal narrowing, but without the sedimentary overlay (the mantle upwelling is exaggerated to compensate), and (3) a crust bulge model, in which crustal thickness increases and protrudes into the mantle, in a manner similar to a mountain root. Still keeping our focus on Lg phenomenology, the results we will be looking at here appear in Figs 18(b), (d) and (f), and in the left panel of Fig. 20.

First, we will compare pinch results with and without sedimentary overlay. The qualitative differences in phase structure observed between Figs 18(b) and (d) are difficult to characterize, though they are visually distinct. It is easier to draw conclusions from the energy curves in Fig. 20, left panel. In this figure, the pinch-with-overlay results are represented by the orange line, and the pinch-without-overlay results are represented by the green line. The first thing to note is that the overall attenuation at the distal end of the model (950 km range) is less severe for the pinch-without-overlay model than for the pinch-with-overlay. In particular, we see that the pinch-without-overlay model experiences an energy reduction of approximately −3 dB with respect to the baseline model, compared with approximately −8 dB for the overlay model. This supports the notion that the sedimentary basin in NSCP 01 is a major component of the loss mechanism in that model, accounting, perhaps, for as much as 5 dB of attenuation. The remainder of the attenuation must be explainable by other mechanisms.

The second thing to note in comparing the pinch models is that both pinch models show an initial upswing in surface energy flux in the anterior tapering wing of the crust variation region, and that both pinch models show a trend of decreasing energy throughout the remainder of the variation region, with the overlay model exhibiting the sharper downtrend, and the non-overlay model exhibiting a more gradual decrease in this region. Most interesting, though, is that whereas the overlay model exhibits a final upswing or recovery of energy at the completion of the crust variation region, the non-overlay model exhibits no such recovery, manifesting a smooth continuation from the posterior tapering wing of the variation region into the region beyond the crustal variation. In the preceding subsection, we proposed that rattling (rapid reverberation) in the very beginning and the tail end zone of the sedimentary basin played a role in the initial and final energy upswings. The absence of this reverberation in the model without the sedimentary overlay, and corresponding lack of final upswing in the energy curve, could be seen as support for the hypothesis that this plays a role in producing the upswing in the overlay model. A second mechanism, however, to explain the final upswing in the overlay model was also proposed. This second mechanism was the division of the Lg phase into two subphases each following a different propagation modality: a sedimentary Lg propagating slowly through the sediment basin (while rapidly attenuating), and the deeper crust Lg propagating with normal velocity, but isolated from interaction with the surface, until reaching the end of the basin where it could again interact with the surface,

explaining the final upswing. This mechanism would also be absent from the non-overlay model, since the thinned crust in that model is positioned at the top of the model, rather than being pushed down to deeper depths by the presence of the sedimentary basin. Thus there would be no sudden energy return event at the conclusion of the crust variation region to produce an upswing of energy. Thus between both proposed mechanisms, we can say that both are likely contributing, though it is not clear without further investigation whether one mechanism is dominant, or whether both contribute significantly to the observed outcomes.

The upswing is present in both models at the beginning of the variation region, however. Here again, two mechanisms were proposed. The first was basin rattling, and the second was a focusing effect from the upward inclination of the crust floor, which would bend rays reflecting off of the floor from a more horizontal orientation to a more vertical orientation, intensifying their interaction with the surface in that region. Basin-rattling is not an option in the non-overlay model. (Although a similar increase in multiple reflections is likely in play.) This leaves the change in incidence angle as the most viable explanation. Note that because the incline of the crust floor in the taper zone is more extreme in the non-overlay model, the intensifying effect could be more extreme. Indeed, the peak (at approximately 350 km) of the non-overlay energy curve is slightly higher than that of the overlay energy curve. It also occurs at a slightly more distant range than in the overlay curve. This could be because both mechanisms (rattling and focusing) are occurring in the overlay model, but only focusing is occurring in the non-overlay model, and the basin-rattling mechanism might be more efficacious in the nearer range window.

The next thing to examine is what happens to the non-overlay energy curve within the fully pinched central region of the crust variation region. As is the case with the overlay model, here we see a generally downwards trend. Unlike the overlay model, however, the downward trend is both (1) not as steep as the overlay model and (2) the energy remains above the baseline curve until the very end of the fully pinched zone (the beginning of the posterior tapering wing). In fact, except for edge effects, the downward trend seems to parallel the baseline within the pinched zone. This may indicate that no additional attenuation mechanisms are in play beyond those also present in the baseline: namely geometric spreading, intrinsic attenuation and a certain amount of continual leakage into the mantle. The fact that the energy level rises above the baseline in this zone may be due to an increase in the rate of surface reflections on account of the shallower crust floor. This is similar to the rattling mechanism of the basin, only it is in basaltic rock media, not lossy sedimentary media. At the conclusion of the pinched region, as the crust begins to broaden back to baseline thickness, the energy level drops again.

Posterior to the crust variation region, the non-overlay energy curve remains below the baseline curve, but above the pinch-with-overlay curve. This indicates that while the pinch-without-overlay had an overall attenuating effect on the Lg phase, it was not nearly as efficient at blocking the Lg as the model with the sedimentary overlay was. This makes sense, since a significant amount of the Lg-blockage mechanism of the overlay model was attributed to the intrinsic attenuation acting on the fraction of the Lg wave that propagated through the sedimentary basin. The remainder of the attenuation was

attributed to mantle leakage as the phase was incident on the anterior tapering wing of the crust modification region, and that mechanism is probably the dominant loss mechanism in the non-overlay model.

4.2.3.5 The bulge model

Last, we turn our attention to the bulge model (NSCP 03). The most striking thing to note is that this is the least disruptive of all the crust variation models. The bulge model traveltime results for Lg propagation appear in Fig. 18(f). At long range, the phase timing, structure and intensity are nearly identical to the baseline, except for a few small pockets of anomalous quiescence. The most striking difference occurs in the middle zone of the crust modification region, (the zone where the crust has expanded to its maximal thickness between the two tapering wings). Here, there is a very sizable quiescence with almost a complete vanishing of energy interacting with the surface.

In the energy curve in Fig. 20, the plum-coloured line represents the bulge result. This figure shows that in the regions beyond the variation region, the bulge result parallels the baseline very closely and manifests only a very minimal attenuation of approximately −1 dB at the terminus of the plot. This tells us that the bulge structure was a very inefficient mechanism for Lg blockage. The majority of the energy propagates through the bulge and retains the majority of its structural and timing characteristics as well.

Within the variation region, a very sharp dip, or notch, is seen in the energy curve. This corresponds with the quiescence zone in the traveltime plot. The mechanism for this is not hard to understand. Since the Lg phase is composed of a wave train of several multiply reflected wave fronts channelled between the surface and the crust floor, there is a substantial amount of interaction with the surface in the region anterior to the variation region. When the Lg phase enters the variation region and the crust thickness expands, the individual wave fronts, after reflecting off the surface, must bottom at a deeper depth before they can return to the surface. The extra time needed to bottom at the deeper depth creates a time window in which the energy is unavailable to interact with the surface. The length of the bulge region is such that when the energy returns to the surface, it has traversed the variation region and continues its original propagation modality.

This would seem to implicate the length of the bulge region as an important parameter in controlling the signal in the bulge region, and perhaps beyond. For example, if the bulge region were sufficiently lengthened, it would be possible for the Lg phase to bottom twice before traversing the region. This should then produce two quiescent zones in the bulge region on the traveltime plot, with an active zone in between, and correspondingly two notches in the energy curve.

It is interesting that the bulge model produced very little terminal-range attenuation, in contrast to the pinch models, especially since mantle leakage as the Lg phase was incident on the inclined crust floor was proposed as a significant attenuation mechanism. An inclined crust floor is not absent from the bulge model, but rather occurs at the end of the variation region rather than the beginning. The results in our model would seem to

indicate that the Lg phase never substantially interacts with this incline. But if the bulge region were lengthened, but not so much as to allow for a double-bottoming, then a substantial interaction with this inclined floor might be possible, and corresponding attenuation of the post-variation region might be observed. Thus we hypothesize that the attenuation measured at the terminus of the model might be controllable and be a cyclical function of the length of the bulge region. This of course could be tested quite easily (but has not as yet been tested).

4.2.3.6 Effects on Pg compared to Lg

The effects on Pg (Figs 19 and 20 right) are for the most part pretty similar to the Lg results (Figs 18 and 20 left). In the baseline traveltime curves, three general differences are notable, and are obviously unrelated to the pinch, bulge or scattering-region structures. One is that the Pn phase is notably excited in the Pg case, whereas the Sn is all but absent in the Lg case. This could indicate that the Moho transition in our model is more leaky to Pg at near-critical incidence angles, allowing a greater fraction of energy into the transition region and upper mantle (Shaw & Orcutt 1984), where the energy can propagate at the faster Pn velocity. The second difference to note is that the series of path multiples making up the Pg wave train seems truncated at a small number beyond approximately 400 km range, in contrast to the much longer wave train that develops in the Lg phase. This may be related to the aforementioned increased transmission into the Moho transition region, which may prevent the Pg phase from supporting the higher-order path multiples. Thirdly is that the Pg phase develops a low energy, long-tailed coda region that expands into a much wider velocity window than what is seen in the Lg case. This is a result of scattering combined with the higher intrinsic *Q* of the *P* propagation mode. Every model we simulated, even if absent any regions of high scattering, does have a very small amount of background heterogeneity (1 per cent) specified in each layer, and although the Pg will experience proportionally less scattering events than the Lg per distance travelled (MFP_P = 13669 km, compared with MFP_S = 6802 km in the baseline crust), those phonons that do scatter will sustain much longer owing to improved intrinsic *Q* of the *P* mode in the crust ($Q_{(int.)P}$=3374 $Q_{(int.)S}$=1500). The effect of that is seen in the mild, but long, coda in the Pg results. Additionally, the *P* to *S* scattering conversion channel is generally much stronger than the *S* to *P* conversion channel (Sato *et al.*, 2012), which explains the energy seen in the Lg velocity window, even absent a distinct Lg phase.

Despite these overall differences in phase presentation, very little differs qualitatively or quantitatively between the Pg and Lg pinch, bulge and scatter results. There is, for the most part, a one-to-one correspondence of graphical features between the traveltime plot and energy curve results from both sets, except for two notable distinctions, to be discussed below. The similarity between Pg and Lg results is perhaps seen most clearly in the energy curve results (Fig. 19). Here, the energy trends for each model case can be seen to be quite similar between Pg and Lg in most respects.

Perhaps the most distinct difference between Pg and Lg visible in the energy curve results is in the overall attenuation at the terminal range of the model (950 km), which can be

seen in Fig. 19 and is also tabulated in Table 4. The attenuation of the Pg phase was less than the attenuation of the Lg phase in each model case. For example, in the pinch-with-overlay model, the Lg phase was attenuated by −8.11 dB at 950 km, whereas the Pg phase in the same model experienced an energy attenuation of only −4.73 dB. Similar reductions in the end range attenuation are seen in all other model cases as well. (Indeed, in the bulge model, the Pg phase actually experiences a very slight amplification at 950 km, compared to −1.54 dB attenuation for Lg.) A simple conclusion to be drawn from this is that the model structures studied here are significantly more efficient Lg blockers than they are Pg blockers.

The second distinct difference to note is visible in the traveltime plots. In the Pg results we see a phenomenon that is absent in the Lg results: mode conversions. Particularly, we see very clear Pg to Lg conversions in the pinch-without-overlay, bulge and scattering-region results, originating from within the variable region. Again, a preferential conversion channel from *P* to *S* for scattering and a significant *P* to *S* reflection coefficient seem to be in play. Even the retrograde backscatter phase in Fig. 19(c), (which is also seen in the Lg case in Fig. 18(c), appearing as a weak reflection off the high-scattering crust region), matches an Lg-like phase velocity, despite being excited by an incident Pg wave. Inclusion of these converted phases in the non-temporally windowed Pg energy curves in Fig. 20 somewhat veils the Pg-blocking activity of the crustal structure. Nevertheless, since the energy is not lost but rather shifted in arrival time, we believe the whole-recording energy curves still provide useful insight, especially when coupled with the traveltime plots.

4.2.3.7 Collisional mountain belt with under-thrusting

Surficial geologic interpretation and reflection profiling of collisional mountain belts often reveal a significantly greater degree of structural complexity associated with collisional mountain belts than that represented by our simple canonical models. Campillo *et al.* (1993), for example, demonstrate that complex over- and under-thrusting of crustal and mantle wedges may explain zones of narrow, overlapping, corridors in efficient and inefficient Lg for paths crossing the Alps. To understand at least some of these effects, we designed the models shown in Fig. 21, consisting of an under-thrust crustal sheet sampled by wavefields incident from either direction of the dipping under-thrust crustal layer. Lg efficiency, inferred from the traveltime plots of Fig. 21 and energy–distance plots in Fig. 22, is similar to the simpler canonical model of crustal thickening (NSCP 03), with end range (950 km) attenuation relative to baseline of −1.94 dB for the case of Lg crossing the collision from the under-thrust side and −1.71 dB for Lg crossing the collision from the over-thrust side, as compared to −1.54 dB for the crust bulge. Directly above the anomalous zone, however, sharp differences in efficiency are seen between the wavefield sampling the structure from the under- or over-thrust side, as well as a fundamental difference in both cases from that of the simple canonical model. For receivers directly above the anomaly with a wavefield arriving from the under-thrust side, Lg is predicted to be less efficient than one arriving from the overthrust side. It should be noted in passing that this experiment with a strike-slip source is not an appropriate test of the elastic reciprocity theorem, in which the input source and

receiver must instead be strictly given in terms of vector components of forces and observed motions (Gangi 1970). Together with the previously cited effects of the length of a zone of crustal thickening, the complexity of Lg amplification and attenuation for sources and receivers within a realistic mountain and the lack of reciprocity of source and receiver positions outside the mountain belt will degrade the reliability of Lg–Q tomographic inversion as a tool for predicting Lg propagation efficiency.

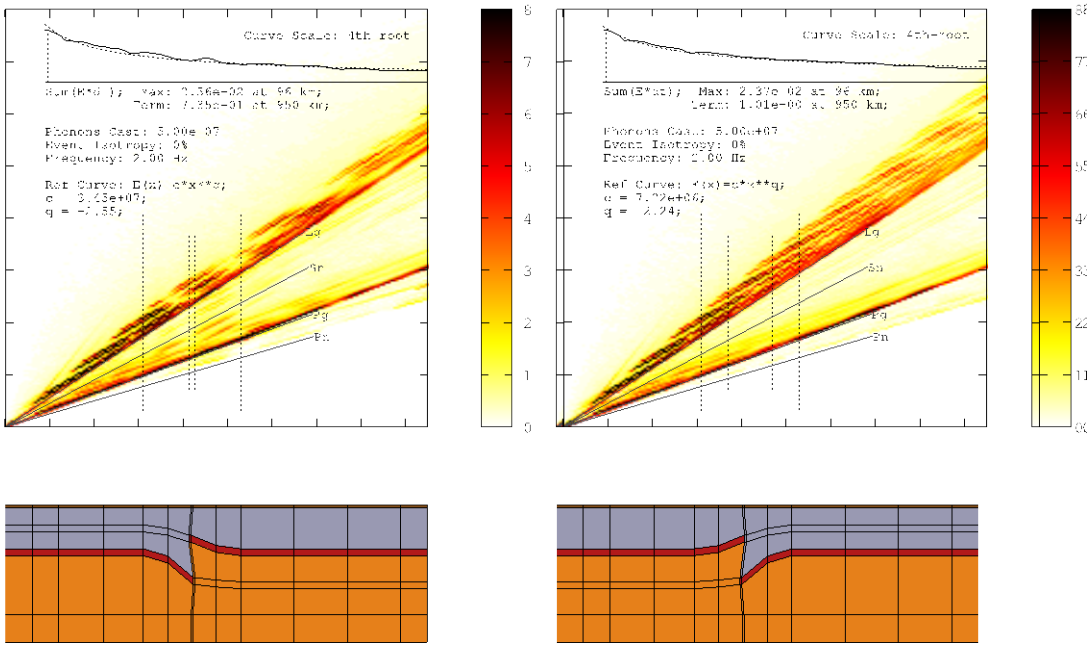

Figure 21. Traveltime curves and model profiles for a collisional mountain belt. *For conditions where up-thrusting slab drift is towards the source (left) and away from the source (right). Source event is an ideal strike-slip earthquake and azimuth is chosen to detect both Pg and Lg phases. Gross model structure is the same as the NSCP models with the exception of additional mesh points through the crust to enable modelling of distinct over- and under-thrusting slabs.*

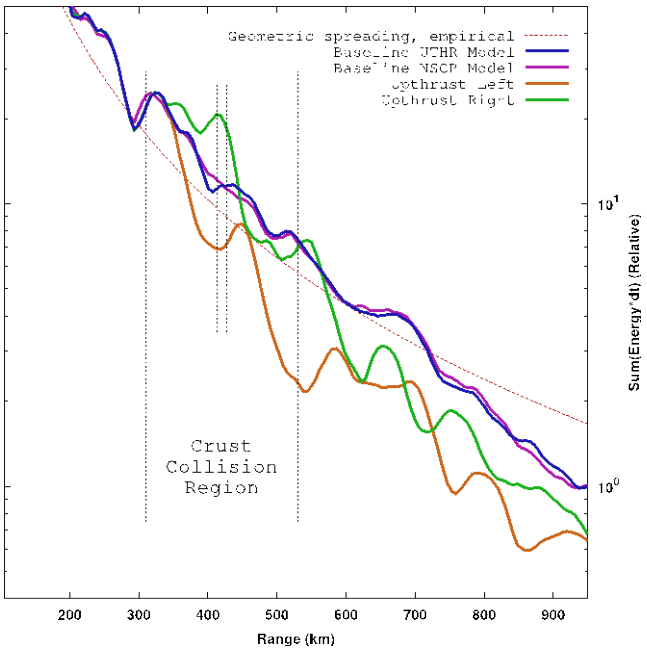

Figure 22. Crustal thickness effects of collisional mountain belt on Lg energy by up-thrust direction. *'Up-thrust left' refers to case where up-thrusting slab is migrating leftwards (towards source) and corresponds the left panel in Fig. 21, and 'Up-thrust right' to the right panel. The baseline condition for the up-thrust models is schematically identical to that of the NSCP models, although with a more intricate mesh structure. Curves represent un-windowed time-integrated all-component energies as a function of distance from source for an azimuth that selects the Lg phase as the initial wave train. End range attenuation relative to baseline for the Up-thrust-left case is −1.94 dB and for the Up-thrust-right case is −1.71 dB.*

4.2.4 Lg and Pg blockage: general conclusions

Previous numerical and observational studies of high-frequency regional seismic propagation have found that phase attenuation and blockage can be due to a combination of factors, for example, Kennett (1986), Maupin (1989) and Sens-Schönfelder *et al.* (2009). These factors include intrinsic attenuation, scattering attenuation, crustal thickness variations, source depth and source mechanism. In this paper we have described the application of a fast, efficient, radiative transport algorithm to the modeling of Lg propagation that allows all of these factors to be included and tested against observations. Some general effects of crustal thickness variations have been demonstrated for several source depths and mechanisms. For earthquakes and explosions at shallow depths in the crustal waveguide having propagation paths crossing crustal thinning regions, Lg is amplified at receivers within the thinned region but strongly disrupted and attenuated at receivers beyond the thinned region. For the same source depths and mechanisms having propagation paths crossing regions of crustal thickening, Lg amplitude is attenuated at receivers within the thickened region, but experiences little or no reduction in amplitude at receivers beyond the thickened region. Localized regions of intense scattering within laterally homogeneous models of the crust increase Lg attenuation but do not disrupt its

coda shape. The effects of crustal thickness variations on Pg correlate with those on Lg, but are much stronger on Lg. In future work, we plan on systematically testing the effects of a broad spectrum of the earth model and source parameters for regional phase paths crossing at least one specific region each of crustal thinning and thickening. These may include regions that have been studied by other investigators, including the North Sea, Barents Sea, Sea of Japan, Tibet Plateau, and the Pyrenees.

4.3. Structural Sensitivities and Parameter Tradeoffs

4.3.1 Structural sensitivity of regional phases

In a simple modeling experiment to determine regional phase sensitivity to depth regions of structure, we omitted any scattering by small-scale heterogeneity and tracked phonons that contributed to regional phase time windows. We saved the deepest model point of penetration for arriving phonons that comprise the time windows of Pn, Pg, Sn, and Lg, color coding those depth regions in the appropriate time windows (Figure 23).

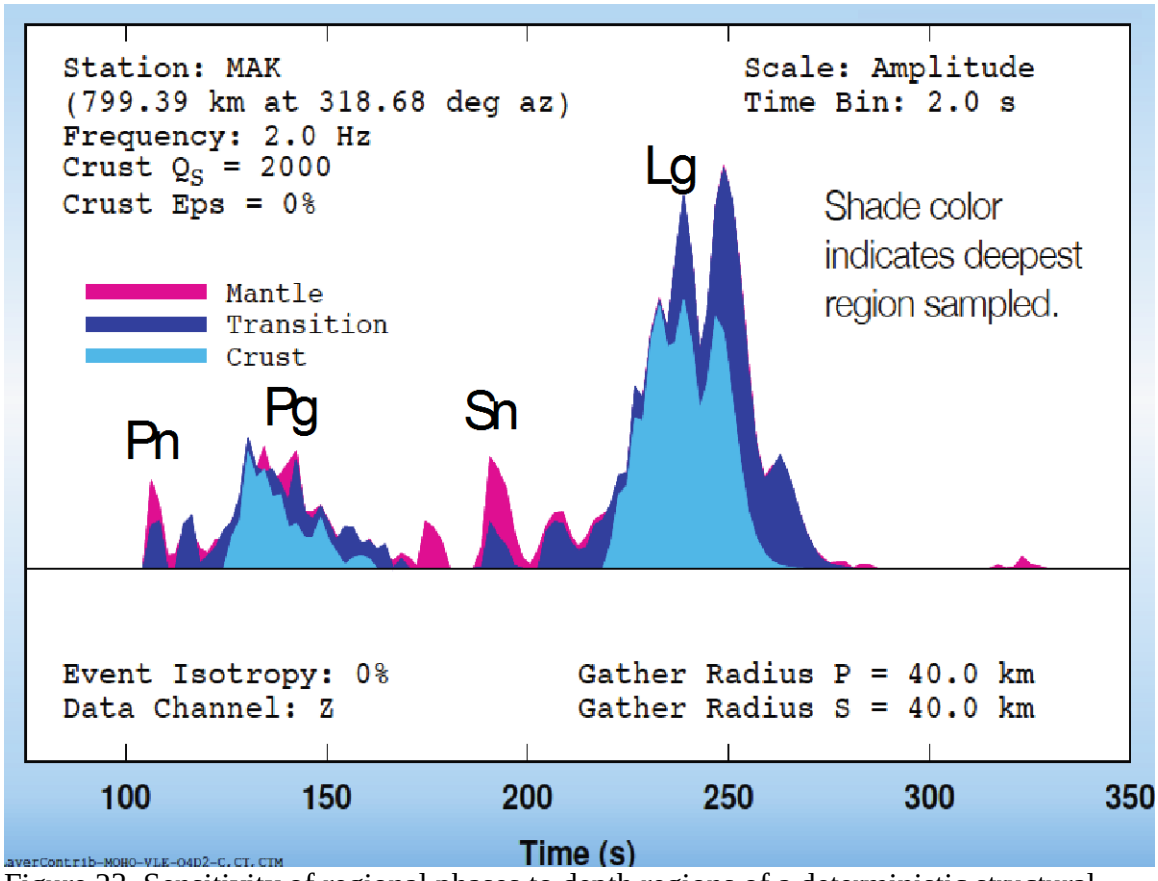

Figure 23. Sensitivity of regional phases to depth regions of a deterministic structural model.

This test confirms that Pg and Lg are strongly sensitive to crustal structure and Pn and Sn to upper mantle structure. Structure of the Moho and details of the transition between crustal and mantle velocities, however, have some effect on all of the important regional phases. The mantle contribution to Pn and Sn phases are from grazing-incidence phonons just under the Moho transition region.

4.3.2 Heterogeneity and intrinsic attenuation tradeoffs

The effects of both scattering and viscoelasticity attenuate regional seismic waves, particularly the Lg waves that propagate as S waves trapped in the crustal waveguide. A challenge in modeling is to eliminate or constrain the tradeoffs between these two forms of attenuation and as well to estimate the parameters and their tradeoffs that shape the spectrum of small-scale heterogeneities. In this paper we apply a radiative transport algorithm that makes it computationally efficient to routinely implement the multiple lapse-time window analysis (MLTWA) to separate scattering from intrinsic attenuation and to identify tradeoffs in parameters describing the structural heterogeneity spectrum.

4.3.2.1 Relating scattering to a heterogeneity spectrum

The reciprocal of the mean free path (eq. 1) is determined by selecting functions g defined in equations 2a-d and integrating over all solid angles $d\Omega$. The example calculation in eq. 1 is that required for determining the mean free path of S waves that are scattered into both P and S waves at the point of scattering.

$$\frac{1}{4\pi}\int (g^{SP} + g^{SS})d\Omega = 1/MFP_S \qquad (1)$$

$$g^{PP}(\psi,\zeta) = \frac{l_0^4}{4\pi}|X_r^{PP}(\psi,\zeta)|^2 \, P\left(\frac{l_0}{\gamma_0}\sin\frac{\psi}{2}\right) \qquad (2a)$$

$$g^{PS}(\psi,\zeta) = \frac{1}{\gamma_0}\frac{l_0^4}{4\pi}|X_\psi^{PS}(\psi,\zeta)|^2 \, P\left(\frac{l_0}{\gamma_0}\sqrt{1+\gamma_0^2-2\gamma_0\cos\psi)}\right) \qquad (2b)$$

$$g^{SP}(\psi,\zeta) = \gamma_0\frac{l_0^4}{4\pi}|X_r^{SP}(\psi,\zeta)|^2 \, P\left(\frac{l_0}{\gamma_0}\sqrt{1+\gamma_0^2-2\gamma_0\cos\psi)}\right) \qquad (2c)$$

$$g^{SS}(\psi,\zeta) = \frac{l_0^4}{4\pi}\left(|X_\psi^{SS}(\psi,\zeta)|^2 + |X_\zeta^{SS}(\psi,\zeta)|^2\right)P\left(2l_0\sin\frac{\psi}{2}\right) \qquad (2d)$$

In eqs 2a-d l_0 is the background S wave number; γ_0 is the ratio of background P to S wave velocity (α_0/β_0); and ψ,ζ are the angles the phonon is deflected upon scattering. The functions X are scattering radiation patterns (Figure 24), which are treated as probability densities for scattering in different directions. The function P is heterogeneity power density spectrum that describes the distribution of heterogeneities of different sizes

relative to an autocorrelation wave number m, where m is given by the arguments of the P's appearing in the g functions. The g functions and associated assumptions follow theory developed in papers by Wu (1985), and discussed in detail in the text by Sato et al. (2012). In the following sub-section we show that an examination of the functional forms of the scattering coefficients (g's) are useful for predicting tradeoffs in the parameters describing the heterogeneity spectrum.

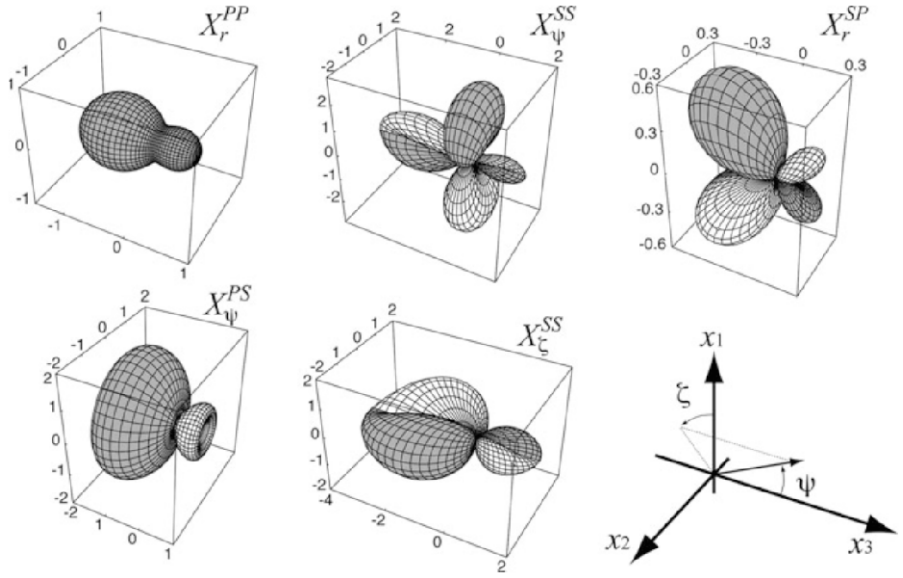

Figure 24. The scattering radiation patterns. *X appearing in the definitions of the scattering coefficients g in eqs. 2a-d. The superscripts PP, PS, SS, and SP denote P scattering into P, P scattering into S, S scattering into S, and S scattering into P respectively.*

The von Kármán spectrum (eq.3) is often used to represent heterogeneities in the crust.

$$P(m) = \frac{8\pi^{3/2}\varepsilon^2 a^3}{(1+a^2m^2)^{\kappa+\frac{3}{2}}} \frac{\Gamma(\kappa+\frac{3}{2})}{\Gamma(\kappa)} \qquad (3)$$

A von Kármán type spectrum is shaped by small number of parameters: ε(fractional P and S velocity fluctuation), and a characteristic scale a after which the spectrum decays with wavenumber at a power κ. The shape parameters that define the power spectrum, especially the corner parameter a via its product with the autocorrelation wavenumber m, can affect path deflection in scattering events as well as the frequency of scattering measured by mean free path. In applications to the Earth's crust, it is commonly assumed that the P and S velocity fluctuations are equal, with density fluctuations scaled to 0.8 times the P and S velocity fluctuations. The assumption $d\ln V_s / d\ln V_P = 1$ simplifies the complexity of the g functions. The assumption for density scaling is largely based on empirical calibrations in the crust, but unlikely to be true in a mantle that is close to neutral buoyancy.

4.3.2.2 Tradeoffs: Heterogeneity Spectrum, Attenuation, and Q

ε *and* a. By examining limiting cases of the product of the corner scale length a and autocorrelation wavenumber m in the von Kármán spectrum, it is possible to predict some tradeoffs in the velocity perturbation parameter ε and corner scale length a that will reproduce nearly identical waveforms in a narrow frequency band. To illustrate this, we chose as a reference the heterogeneity spectrum inferred from radiative transport modeling of a series of narrow-band waveforms from a Lop Nor, China earthquake (Figures 9 and 10). When the product am is much less than 1 $(am << 1)$, any combination of $\varepsilon^2 a^3$ equal to a constant should result in the same power spectrum P, scattering coefficients g, and seismograms. When am is much greater than 1 $(am >> 1)$, any combination such that ε^2 / a is constant should likewise result in the same power spectrum, P, scattering coefficients g, and seismograms. For the case when am is on the order of 1, any combination such that $\varepsilon^2 a$ is constant should result in approximately the same seismogram. This is illustrated for the *am*=1 domain for the modeled Lop Nor earthquake in Figure 25 for a 2 Hz seismogram. Note that as the mean free path of scattered S waves (S-MFP) increases, a measure of forward versus back scattering (S-DP) decreases. This is a simple consequence that energy can be redistributed from a pulse to later times, lengthening coda, by two different mechanisms: (1) either changing the number of times a wave is scattered, or (2) changing the magnitude of the angular deflection in each scattering event.

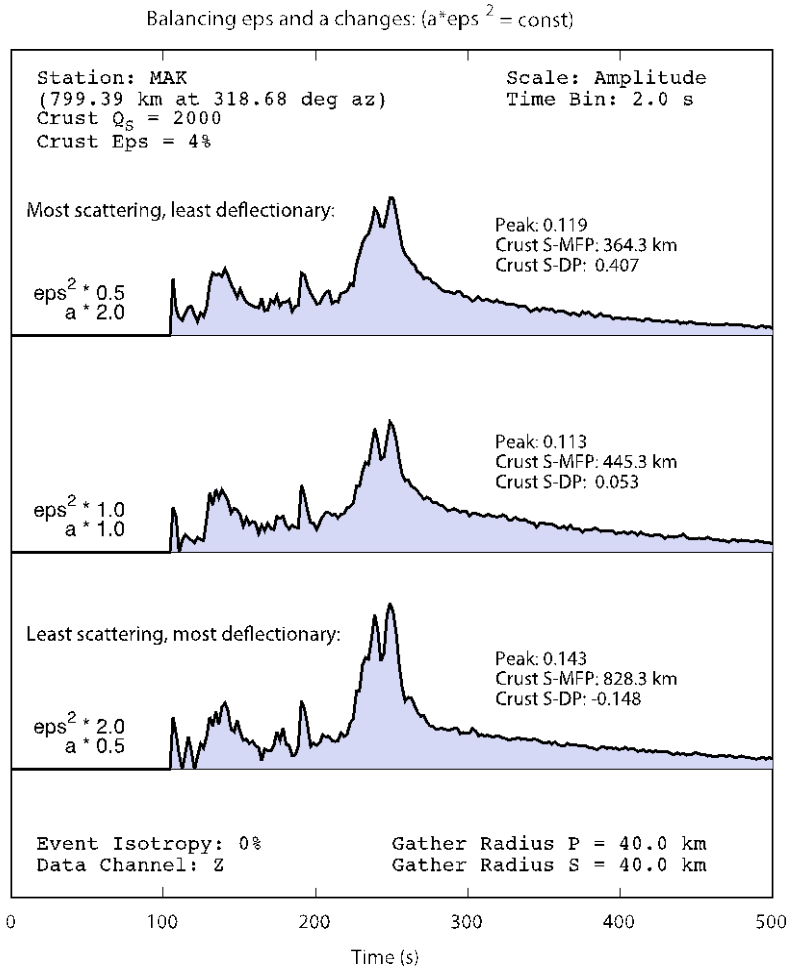

Figure 25. Synthetic envelopes at 2 Hz illustrating tradeoffs between a (the parameter that controls the corner wavenumber of a von Kármán heterogeneity spectrum), eps, (the fractional fluctuation in P and S velocity), and Q (intrinsic attenuation).

Intrinsic Qs and frequency. The effect of intrinsic attenuation applied to a narrow band seismogram will attenuate the energy of each S wave traveling time T by a factor $\exp(-\omega T/Q)$. Hence, it is possible to produce identical seismograms, varying frequency and intrinsic attenuation by the same factors. Figure 26 illustrates this effect, comparing 2 Hz seismograms varying intrinsic Q, against seismograms at the right, in which Q is held constant but frequency is varied. From top to bottom of both panels, the product $\varepsilon^2 a$ varies from ¼ to 4, strongly affecting the of shapes of the seismogram envelopes, decreasing the mean free path, and moving the wavefield into a regime in which single scattering dominates into one in which multiple scattering dominates. These regimes are probed by varying ε, a, and Q at a constant frequency in the left panel but by varying ε, a, and frequency in the right panel. A conclusion that can be made from this is that modeling in a series of frequency bands will tend to sample at least the boundaries of a scattering domain, if not cross several scattering domains, and minimize tradeoffs between parameters of the heterogeneity spectrum and intrinsic attenuation.

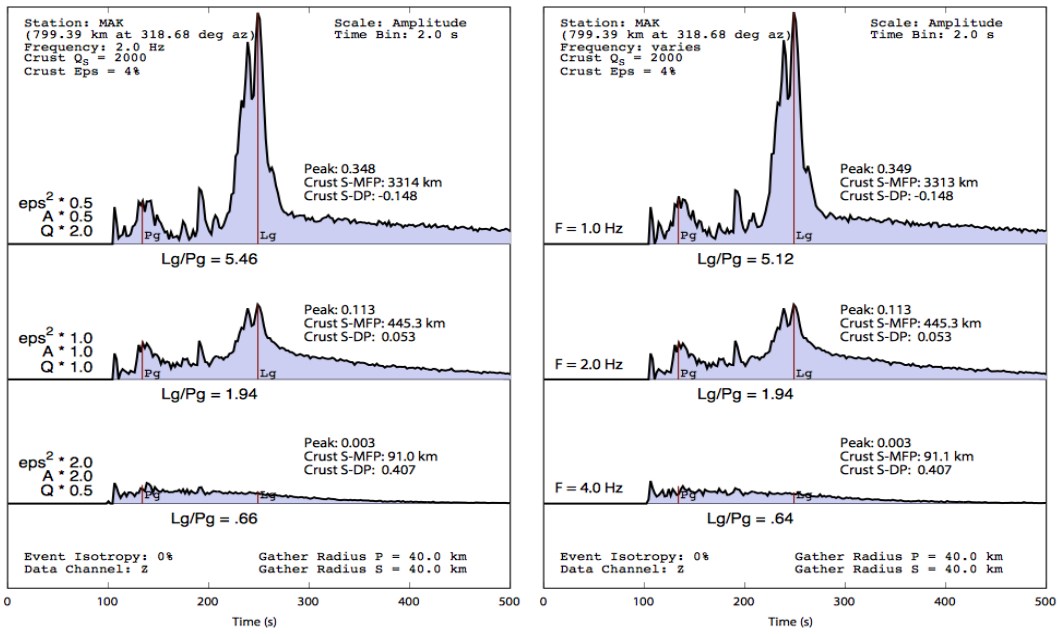

4

Figure 26. Varying eps, a, and Q by certain factors is equivalent to varying the frequency band of observation. *Frequency is constant in the left column, while eps, a, and Q vary; frequency varies in the right column, while eps, a and Q remain constant.*

4.3.3 Multiple Time Lapse Window Analysis

With radiative transport modeling we examined the multiple lapse time window analysis (MLTWA) of Hoshiba (1993) and Fehler et al. (1992) to separate the effects of intrinsic attenuation from scattering attenuation. The method consists in measuring ratios of energy at different distances and time windows (Figure 27 and eqs.4ab). Both scattering and intrinsic attenuation reduce energy at longer distance compared to shorter distance. Only scattering, however, delays energy, shifting it into later time windows. It is this difference that is exploited in the MLTW measurements.

$$R1 = \log_{10}\left[\frac{E_{early,\,far}}{E_{late,\,far}}\right] \qquad (4a)$$

$$R2 = \log_{10}\left[\frac{r_{near}^{\eta}\,E_{early,\,near}}{r_{far}^{\eta}\,E_{early,\,far}}\right] \qquad (4b)$$

A complete formulation of the MLTWA corrects for geometric spreading when computing these energy ratios. This is indicated by the factor r for distance raised to a power η in the eqs. 4a,b. Applied to the Lg wave, the η power is best determined from the distance decay of a synthetic Lg envelope in a model in which scattering and intrinsic attenuation is absent. The ratio R2 is sensitive to both intrinsic and scattering attenuation, which can be used to infer a total apparent attenuation Q_{total}^{-1}, where $Q_{total}^{-1} = Q_{scat}^{-1} + Q_{\text{int}}^{-1}$.

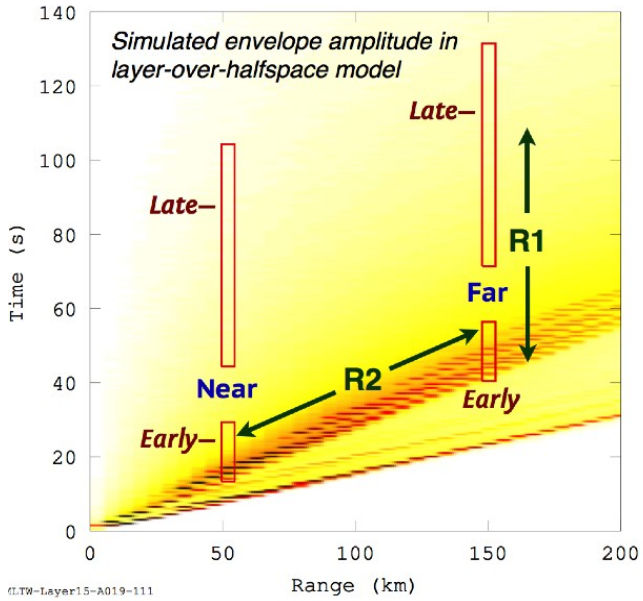

Figure 27. Definition of the R1 and R2 energy ratios used in MLTWA. *The definition of the R1 and R2 energy ratios used in the multiple lapse-time window method for separating scattering and intrinsic attenuation.*

It is important to note that this total attenuation, which includes the effects of intrinsic attenuation and multiple scattering, is related to but not equivalent the Qscat of Aki (1969) and Aki and Chouet (1975). These early studies and a voluminous number of Q_{scat} measurements made since neglect multiple scattering and assume that S codas are largely shaped by single scattering. Multiple scattering, which is included in radiative transport modeling, becomes increasingly important as frequency and range increase. In the Earth at higher frequency ≥ 5 Hz) multiple scattering can shape a complete waveform into a continuous spindle, best predicted by a diffusion process, making it impossible to separate individual regional phases (e.g., 4 Hz envelope in Figure 10).

Scattering attenuation, both single and multiple, decreases the R1 ratio by increasing the amplitude of late far coda. Intrinsic attenuation, however, always increases R1 by decreasing the late far coda. For a fixed corner scale a of a von Kármán spectrum, we stepped through a series of 81 pairs of velocity fluctuation ε and intrinsic Q values to create a mesh of values in R1 and R2 space. By plotting R2 against R1, intrinsic and scattering attenuation may be separated as illustrated in Figure 28. (R1,R2) points are determined from measurements of synthetic coda envelopes for a near station at 50 km and far station at 150 km computed from the Lg coda in a model consisting of a crustal layer over a halfspace. We chose a relatively thin crust of 15 km to enable development

of a true Lg wave composed of multiply interfering S waves at shorter ranges. A shallow strike-slip source is assumed and the near and far stations are taken along the azimuth in which S wave radiation is maximum (e.g., Sanborn and Cormier, 2018). Although the computation time of the simulations consumed 840 hours with 7 cores, a similar exploration of the two parameters ε and Q_{int}^{-1} would have consumed several orders of magnitude more computation time by 3-D finite difference modeling. Gray lines connect points having a constant intrinsic attenuation. Since the R2 measurements determine a Q_{total}^{-1}, values of Q_{scat}^{-1} are determined by subtracting Q_{int}^{-1} from Q_{total}^{-1}. Colored lines connect points having constant Q_{scat}^{-1}. The yellow shaded band marks a region of (R1,R2) space where intrinsic and scattering Q are approximately equal. We rely on this band to calibrate the mesh and to more accurately estimate lines of constant Q_{scat} because Q_{scat} cannot be stably defined by mean free paths.

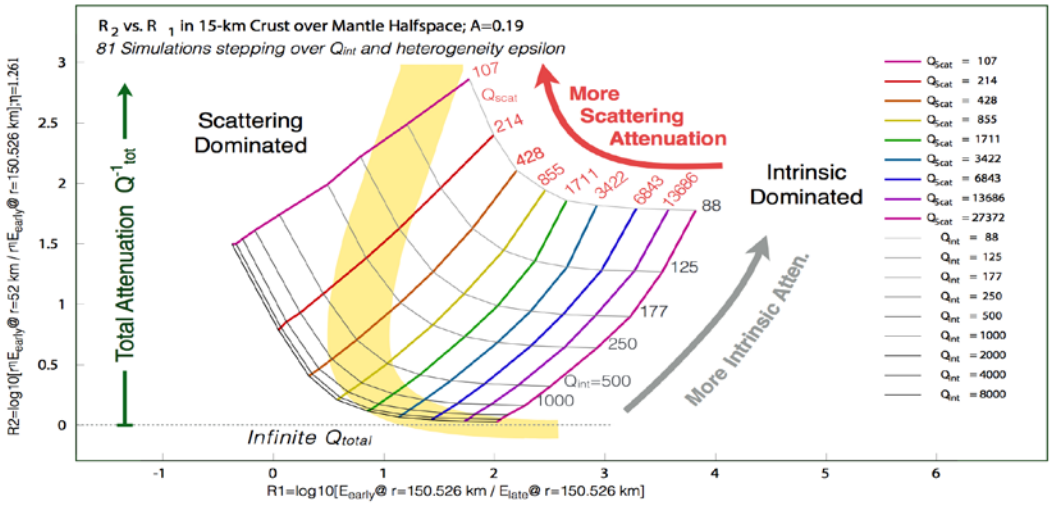

Figure 28. (R1,R2) mapping obtained by integrating elastic S and Lg energy in near and far and early and late time windows from 81 radiative transport simulations envelopes.

4.3.3.1 Relation of Qscat to MFP

Having a strategy to separate Q_{scat} from its contribution to Q_{total}, it is desirable to have a physical understanding of what Qscat, actually measures. The time decay of R1 from Q_{total} is determined is a measure of elastic energy integrated over a short time window. A dimensionless time constant Qscat controls the portion of the exponential decay of R1 that is induced by scattering. Scattering removes energy from the early time

window that defines R1, sending it to later times and places. The decay of this integrated energy due to scattering can be thus defined by

$$E(r,t) = \bar{E}(r,t)e^{-\omega t/Q_{scat}} \qquad (5).$$

Note that the choice of the early time window will clearly affect the value of Q_{scat}. For the integrated energy of an S wave coda or the S waves that comprise an Lg coda, we can define an extinction length Λ_{scat}, over which the magnitude of the time-integrated lump of energy decays by e^{-1} due to the effects of scattering,

$$\Lambda_{scat} = \frac{\beta}{\omega} Q_{scat} \qquad (6).$$

The extinction length is not equivalent to the mean free path $(\Lambda_{scat} \neq MFP)$ because scattering can also remove energy from early time windows by shifting it into different azimuths. We can, however, use MLTW simulations to establish a proportionality between Λ_{scat} and MFP. By examining the effects of the trig functions that appear in the power spectra of the g scattering coefficients (eq.2a-d) and the corner parameter a in the definition of the von Kármán spectrum, we can see that the directionality of scattering depends on the spectrum corner scale relative to the wavelength λ. A directional radiance (forward scattering power as a function of angular deflection) can be plotted as shown in figure 29 for different values of the ratio λ / a. Then, using radiative transport the output of mean free path and an estimate of Qscat from the application of MLTW to predicted (R1, R2) radiative transport mappings, we can solve for the this proportionality constant. Figure 29 shows that path deflections decrease and the proportionality constant increases as the corner scale a increases. All three scattering regimes from which the figure 10 calculations were done have the same Q_{scat}, but many narrow-angle deflections ($\Lambda_{scat} = 23\, MFP$ at $\frac{a}{\lambda} = 0.11$) are needed to remove the same energy from an early time window as a single wide angle scatterer ($\Lambda_{scat} = 1.73\, MFP$ at $\frac{a}{\lambda} = 0.98$ a/L = 0.98). This illustrates another example of the ε and a tradeoff since ε controls the rate scattering events.

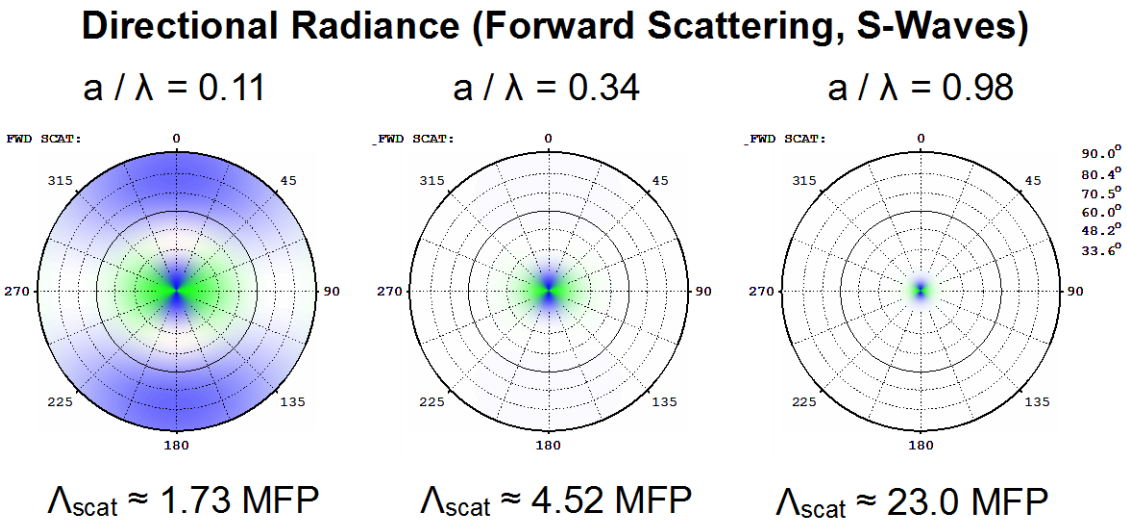

Figure 29. Directional radiance mapped by azimuthal and vertical angle deflections at scattering points determined from radiative transport simulations. *The corner parameter in a von Kármán spectrum is varied and relations are determined between the scattering extinction length $\Lambda_{s\ cat}$ and MFP (mean free path).*

4.3.3.2 Strategy for Minimizing the ε and a Tradeoff

Although the value of Q_{scat} can depend on the length of the time window used for computing integrated energy and different combinations of ε and a can produce the same Q_{scat} it is possible to eliminate the tradeoff between ε and a by applying MLTW analysis to (R1,R2) maps for a small number of narrow bandpassed frequencies. The frequency (wavelength) at which Q_{scat} is maximum will occur when the corner parameter a is on the order of wavelength. Figure 30 demonstrates attenuation measured by peak amplitude decay of Pg and Lg codas occurs when ka is close to 1 For a either much less or much greater than this value, scattering attenuation measured by Q_{scat}^{-1} is low. When a is much less than a wavelength, scattering events are infrequent and Q_{scat}^{-1} is low. When a is much greater than wavelength, scattering is frequent but involves much less angular deflection and Q_{scat}^{-1} is also low. A method to determine a would be to compute R1 and R2 for a range of frequencies, determining Q_{scat}^{-1} and Q_{int}^{-1} for each frequency from computed (R1,R2) maps. From these measurements seek the frequency where the seismic albedo B_0 (eq.7) is a maximum.

$$B_0 = \frac{Q_{scat}^{-1}}{Q_{scat}^{-1} + Q_{\text{int}}^{-1}} \qquad (7)$$

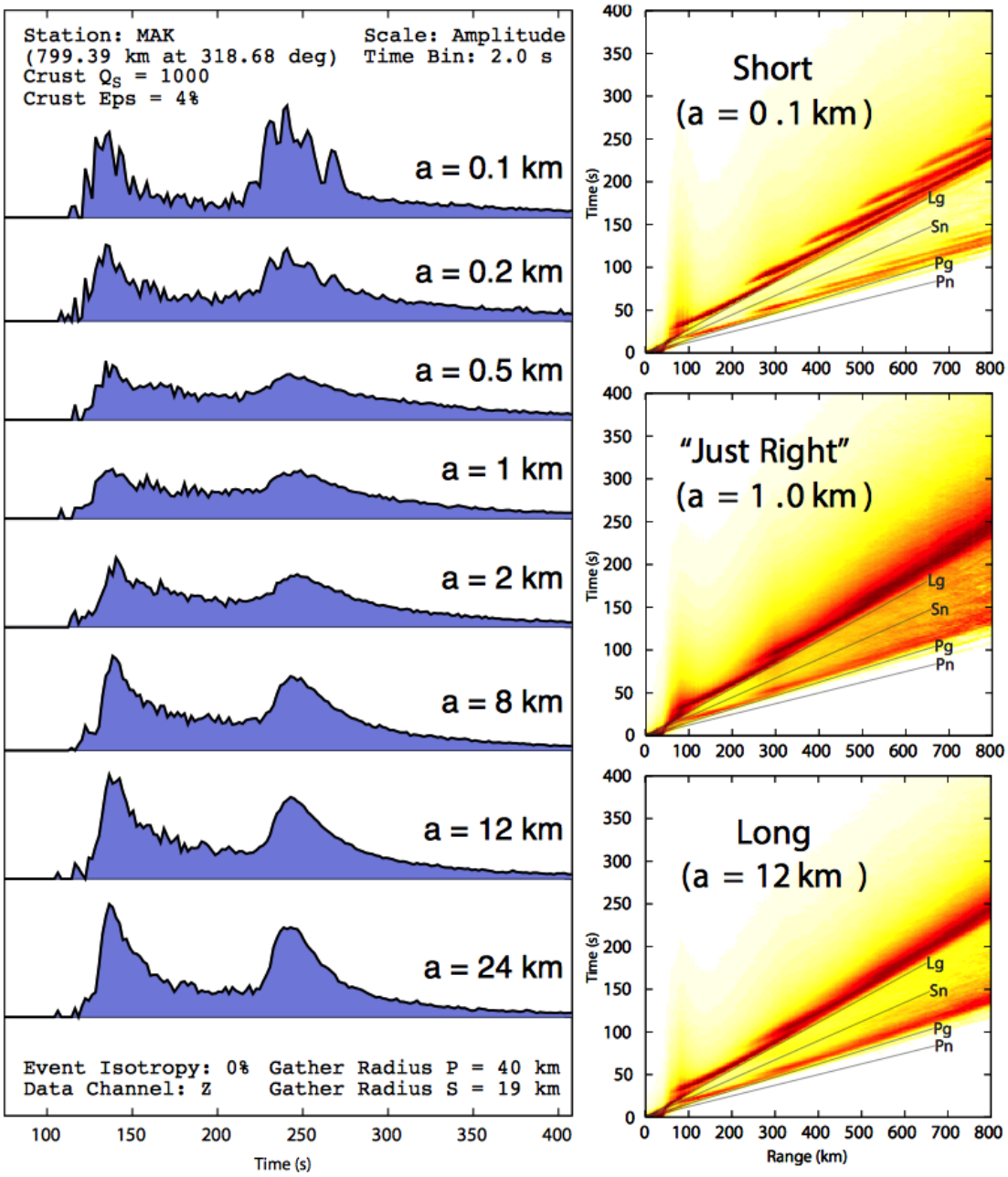

Figure 30. The corner parameter a can be determined by finding the wavelength (frequency) at which the seismic albedo $(Q_{scat}^{-1} / Q_{total}^{-1})$ is maximum using a series of narrow bandpassed waveforms.

Once the a parameter is determined, the velocity fluctuation parameter ε can determined from the proportionality between the extinction coefficient and mean free path of for the simulation that best matches the waveform in the frequency band having peak albedo.

4.3.4 Parameter Tradeoffs: general conclusions

The unknowable small-scale heterogeneity in the modeling of high frequency regional seismograms involves challenges in constraining even a small number of parameters that describe the shape of a statistically described heterogeneity spectrum. We have suggested procedures for measuring and separating intrinsic from scattering attenuation and constraining tradeoffs in parameters describing the crustal heterogeneity spectrum. We have focused our study on the effect of that spectrum on the shape of the S coda, which at longer range evolves into a series of S waves multiply reflected between Earth's surface and Moho, commonly known as the Lg wave. We assume a von Kármán spectrum of crustal heterogeneity described by 3 parameters, a P velocity fluctuation that equals the S velocity fluctuation, and a density fluctuation that scales as 0.8 times that of the velocity fluctuations. Heterogeneity is assumed to be spatially isotropic, but the radiation patterns of scattered elastic waves are anisotropic, with angularly varying lobes of energy in forward and backward directions. Many of these assumptions can be relaxed as needed, but with the starting point of analysis still begins with syntheses of waveforms in multiple narrow pass bands in frequency, measuring time-integrated windows of energy to characterize the shapes of the waveforms in different time windows and different distances, an example of which is the multiple time-lapse window method (MLTWA). In each frequency band for a fixed starting assumption of velocity fluctuation e the space of (R1,R2) energies of the MLTWA method are mapped for varying corner parameter a.
Qscat and Q int are determined from comparing the obsverved (R1,R2)
from a seismogram to the best fitting location in the synthetic (R1,R2) map.

Our demonstrations have assumed a known or well-constrained source radiation pattern. The modeling schemes can be adapted to situations in which source mechanisms are unknown using methods first described in Fehler et al. (1992), where energy envelopes are integrated for multiple events at fixed distance intervals in three successive time windows, each normalized by the energy envelope of each event in a late time window. Alternative schemes to (R1,R2) mapping for separating intrinsic and scattering attenuation and estimating of extinction length in multiple frequency bands (e.g, Del Pezzo, et al, 2011) are also facilitated by fast radiative transport algorithms for synthesizing waveform envelopes.

Q_{int} does not depend on time window length used in MLTWA and is a fundamentally valuable parameter to retrieve for comparison with laboratory measurements and theoretical predictions for real crustal materials. Q_{scat}, however, is related to an extinction length that depends on the length of time windows used in MLTW. Q_{scat} is affected by both mean free path length as well as by the angular deflections that occur at each scatterer, and strongly depends on two parameters, a and ε, of the von Kármán spectrum. The ε velocity fluctuation parameter trades off with the corner parameter a of the von Kármán spectrum. This tradeoff can be minimized by finding the frequency band in which the albedo of a waveform envelope is maximized at ka = 1. In this band, the squared product of the velocity fluctuation parameter times a can produce identical waveforms. Once a has been fixed by finding the a producing maximum albedo, ε can be determined from the best fitting envelope to data in the band in which ka=1.

REFERENCES

Aki, K., "Analysis of the seismic coda of local earthquakes as scattered waves," *J. Geophys. Res.*, **74(2)**, 1969, pp. 615–631.

Aki, K. and Chouet, B., "Origin of coda waves: Source, attenuation, and scattering effects," *J. Geophys. Res.*, **80(23)**, 1975, pp. 3322–3342.

Brune, J., "Tectonic stress and the spectra of seismic shear waves from earthquakes," *J. Geophys. Res*., **75**, 1970, pp. 4997-5009.

Bukchin, B. G., Mostinsky, A. Z., Egorkin, A. A., Levshin, A. L., and Ritzwoller, M. H., "Isotropic and nonisotropic components of earthquakes and nuclear explosions on the Lop Nor test site, China," *Pure Appl. Geophys.*, **158**, 2001, pp. 1497–1515.

Campillo, M., "Lg wave propagation in a laterally varying crust and the distribution of the apparent quality factor in central France," *J. Geophys. Res.*, **92(B12)**, 1987, pp. 12,604–12,614.

Campillo, M., Feignier, B., Bouchon, M., and Bethoux, N., "Attenuation of crustal waves across the Alpine Range," J. *Geophys. Res.*, **98 (B2)**, 1993, pp. 1987–1996.

Cao, S. and Muirhead, K.J., "Finite difference modelling of Lg blockage," *Geophys. J. Int.*, **115(1)**, 1993, pp. 85–96.

Cerveny, V. and Ravindra, R., *Theory of Seismic Head Waves*, 1971, University of Toronto Press.

Chazalon, A., Campillo, M., Gibson, R., and Carreno, E., "Crustal wave propagation anomaly across the Pyrenean Range: Comparison between observations and numerical simulations," *Geophys. J. Int.*, **115(3)**, 1993, pp. 829–838.

Contrucci, I., Nercessian, A., Bethoux, N., Mauffret, A., and Pascal, G., "A Ligurian (Western Mediterranean Sea) geophysical transect revisited," *Geophys. J. Int.*, **146 (1)**, 2001, pp. 74–97.

Cormier, V. F. and Anderson, T. S., "Efficiency of Lg propagation from SmS dynamic ray tracing in three-dimensionally varying crustal waveguides," *Pure Appl. Geophys.*, **161(8)**, 2004, pp. 1613–1633.

Del Pezzo, E., Bianco, F., Marzorati, S., Augliera, P., D'Alema, E., and Massa, M., "Depth-dependent intrinsic and scattering seismic attenuation in north central Italy," *Geophys. J. Int.*, **186 (1)**, 2011, pp. 373-381.

Fehler, M., Hoshiba, M., Sato, H., and Obara, K., "Separation of scattering and intrinsic attenuation for the Kanto-Tokai region, Japan, using measurements of S-wave energy versus hypocentral distance," *Geophys. J Int.*, **108(3)**, 1992, pp. 787–800.

Fisk, M. D., "Source spectral modeling of regional P/S discriminants at nuclear test sites in China and the former Soviet Union," *Bull. Seism. Soc. Am.*, **96(6),** 2006, pp. 2348–2367.

Furumura, T. and Kennett, B.L.N., "Variations in regional phase propagation in the area around Japan," *Bull. Seism. Soc. Am.*, **91 (4)**, 2001, pp. 667–682.

Furumura, T., Hong, T.-K., and Kennett, B.L.N., "Lg wave propagation in the area around Japan: observations and simulations," *Prog. Earth Planet. Sci.*, **1(10)**, 2014, pp. 1–20.

Gangi, A.F., "A derivation of the seismic representation theorem using seismic reciprocity," *J. Geophys. Res.*, **75 (11)**, 1970, pp. 2088–2095.

Goff, J. A., Holliger, K., and Levander, A., "Modal fields: A new method for characterization of random seismic velocity heterogeneity," *Geophys. Res. Lett*., **21(6)**, 1994, pp. 493–496.
Grad, M., Tiira, T., and ESC Working Group, "The Moho depth map of the European Plate," *Geophys. J. Int.*, **176(1)**, 2009, pp. 279–292.
Gregersen, S., "Lg-wave propagation and crustal structure differences near Denmark and the North Sea," *Geophys. J. Int.*, **79(1)**, 1984, pp. 217–234.
Gudmundsson, Ó. and Sambridge, M., "A regionalized upper mantle (RUM) seismic model," *J. Geophys. Res*., **103(B4)**, 1998, pp. 7121–7136.
Gusev, A. A. and Abubakirov, I. R., "Monte-Carlo simulation of record envelope of a near earthquake," *Phys. Earth Planet. Inter*., **49(1–2)**, 1987, pp. 30–36.
Hoshiba,M., "Separation of scattering attenuation and intrinsic absorption in Japan using the multiple lapse time window analysis of full seismogram envelope," *J. Geophys. Res.*, **98(B9)**, 1993, pp. 15809–15824.
Hoshiba, M., "Seismic coda wave envelope in depth-dependent S wave velocity structure," *Phys. Earth Planet. Inter.*, **104(1–3)**, 1997, pp. 15–22.
Keers, H., Nolet, G., and Dahlen, F.A., "Ray theoretical analysis of Lg," *Bull. Seism. Soc. Am.*, **86(3)**, 1996, pp. 726–736.
Kennett, B., Engdahl, E., and Buland, R., "Constraints on seismic velocities in the Earth from travel times," *Geophys. J Int*., **122(1)**, 1995, pp. 108–124.
Kennett, B.L.N.," Lg waves and structural boundaries," *Bull. Seism. Soc. Am.*, **76 (4)**, 1986, pp. 1133–1141.
Laske, G., Masters, G., and Reif, C., "Crust 2.0: A new global crustal model at 2x2 degrees," http://igppweb.ucsd.edu/~gabi/crust2.html, 2011.
Levander, A., England, R., Smith, S., Hobbs, R., Goff, J., and Holliger, K., "Stochastic characterization and seismic response of upper and middle crustal rocks based on the Lewisian gneiss complex, Scotland," *Geophys. J. Int.*, **119(1)**, 1994, pp. 243–259.
Margerin, L., "Introduction to radiative transfer of seismic waves," in *Seismic Earth: Array Analysis of Broadband Seismograms*, eds. Levander, A. and Nolet, G., American Geophysical Union, Washington, DC, 2005, pp. 229–252,
Margerin, L. and Nolet, G., "Multiple scattering of high-frequency seismic waves in the deep Earth: Modeling and numerical examples," *J. Geophys. Res.*, 2003, **108(B5),** doi:10.1029/2003JB002455.
Margerin, L., Campillo, M., and Tiggelen, B. V., "Monte Carlo simulation of multiple scattering of elastic waves," *J. Geophys. Res.*, **105(B4)**, 2000, pp. 7873–7892.
Martynov, V. G., Vernon, F. L., Mellors, R. J., and Pavlis, G. L., "High-frequency attenuation in the crust and upper mantle of the northern Tien Shan," *Bull. Seism. Soc. Am.*, **89(1)**, 1999, pp. 215–238.
Maupin, V., "Numerical modelling of Lg wave propagation across the North Sea Central Graben," *Geophys. J. Int.*, **99(2)**, 1989, pp. 273–283.
McNamara, D.E. and Walter, W.R., "Mapping crustal heterogeneity using Lg propagation efficiency throughout the Middle East, Mediterranean, Southern Europe and Northern Africa," *Pure Appl. Geophys*., **158(7)**, 2001, pp. 1165–1188.

Mendi, C.D., Ruud, B.O., and Husebye, E.S., "The North Sea Lg-blockage puzzle," *Geophys. J. Int.*, **130(3)**, 1997, pp. 669–680

Mueller, R.A. and Murphy, J.R., "Seismic characteristics of underground nuclear detonations," *Bull. Seism. Soc*. **61(6)**, 1971, pp. 1675-1692.

Obermann, A., Planès, T., Larose, E., Sens-Schönfelder, C., and Campillo, M., "Depth sensitivity of seismic coda waves to velocity perturbations in an elastic heterogeneous medium," *Geophys. J. Int.*, **194(1)**, 2013, pp. 372–382.

Pedersen, H. A., Avouac, J.-P., and Campillo, M., "Anomalous surface waves from Lop Nor nuclear explosions: Observations and numerical modeling," *J. Geophys. Res.*, **103(B7),** 1998, pp. 15051–15068.

Phillips, W., Hartse, H., Taylor, S., Velasco, A., and Randall, G., "Regional phase amplitude ratio tomography for seismic verification," Los Alamos National Laboratory, NM, 1999, Tech. rep., LAUR-99-1904.

Przybilla, J., Wegler, U., and Korn, M., "Estimation of crustal scattering parameters with elastic radiative transfer theory," *Geophys. J Int.*, **178(2)**, 2009, pp. 1105–1111.

Pullammanappallil, S., Levander, A., and Larkin, S. P., "Estimation of crustal stochastic parameters from seismic exploration data," *J. Geophys. Res.*, **102(B7)**, 1997, pp. 15269–15286.

Rachman, A. N. and Chung, T. W., "Depth-dependent crustal scattering attenuation revealed using single or few events in South Korea," *Bull. Seism. Soc. Am.*, **106(4)**, 2016, pp. 1499–1508.

Rodgers, A.J., Ni, J.F., and Hearn, T.M., "Propagation characteristics of short-period Sn and Lg in the Middle East," *Bull. Seism. Soc. Am.*, **87(2)**, 1997, pp. 396–413.

Sanborn, C.J., Cormier, V.F., and Fitzpatrick, M., "Combined effects of deterministic and statistical structure on high-frequency regional seismograms," *Geophys. J. Int.*, **210(2)**, 2017, pp. 1143-1159.

Sanborn, C.J. and Cormier, V.F., "Modelling the blockage of Lg waves from three-dimensional variations in crustal structure," Geophys. J. Int., 214(2), 2018, pp. 1426- 1440.

Sato, H., Fehler, M.C., and Maeda, T., *Seismic Wave Propagation and Scattering in the Heterogeneous Earth*, 2nd edition, Springer-Verlag, 2012.

Sens-Schonfelder, C., Margerin, L., and Campillo, M., "Laterally heterogeneous scattering explains Lg blockage in the Pyrenees," *J. Geophys. Res.*, **114(B7)**. 2009, B07309.

Shapiro, N., Bethoux, N., Campillo, M., and Paul, A., "Regional seismic phases across the Ligurian Sea: Lg blockage and oceanic propagation," *Phys. Earth Planet. Inter*., **93(3-4)**, 1996, pp. 257–268.

Shaw, P. and Orcutt, J., "Propagation of PL and implications for the structure of Tibet," *J. Geophys. Res.*, **89(B5)**, 1984, pp. 3135–3152

Shearer, P. M. and Earle, P. S., "Observing and modeling elastic scattering in the deep Earth," in *Advances in Geophysics*, Volume 50: Earth Heterogeneity and Scattering Effects on Seismic Waves, ed. Fehler, H.S.M., Elsevier, 2008.

Sykes, L. R. and Nettles, M., "Dealing with hard-to-identify seismic events globally and those near nuclear test sites," in Poster presented at the International Scientific Studies Conference, Comprehensive Nuclear-Test-Ban Treaty Organization, Vienna, Austria, 2009.

Vaccari, F. and Gregersen, S., "Physical description of Lg waves in Inhomogeneous Continental crust," *Geophys. J. Int.*, **135(2)**, 1998, pp. 711–720.

Wu, R.-S., "Multiple scattering and energy transfer of seismic waves—separation of scattering effect from intrinsic attenuation—I. Theoretical modeling," *Geophys. J. Int.*, **82 (1)**, 1985, pp. 57–80.

Wu, X.-Y. and Wu, R.-S., "Lg-wave simulation in heterogeneous crusts with surface topography using screen propagators," *Geophys. J. Int.*, **146 (3)**, 2001, pp. 670–678.

Yoshimoto, K., "Monte Carlo simulation of seismogram envelopes in scattering media," *J. Geophys.Res.*, **105(B3)**, 2000, pp. 6153–6161.

Zhang, T.-R. and Lay, T., "Why the Lg phase does not traverse oceanic crust," *Bull. Seism. Soc. Am.*, **85(6)**, 1995, pp. 1665–1678.

List of Symbols, Abbreviations, and Acronyms

AFRL	Air Force Research Laboratory
AFSPC	Air Force Space Command
LANL	Los Alamos National Laboratory
IMS	International Monitoring System
MLTWA	Multiple Lapse-Time Window Analysis

DISTRIBUTION LIST

DTIC/OCP
8725 John J. Kingman Rd, Suite 0944
Ft Belvoir, VA 22060-6218 1 cy

AFRL/RVIL
Kirtland AFB, NM 87117-5776 1 cy

Official Record Copy
AFRL/RVBYE/Dr. Frederick Schult 1 cy

This page is intentionally left blank.